JHEP

Published for SISSA by Springer

Received: *July 22, 2021*
Accepted: *September 15, 2021*
Published: *October 13, 2021*

NLO EW and QCD corrections to polarized ZZ production in the four-charged-lepton channel at the LHC

Ansgar Denner and Giovanni Pelliccioli

Institut für Theoretische Physik und Astrophysik, Universität Würzburg, Emil-Hilb-Weg 22, 97074 Würzburg, Germany

E-mail: ansgar.denner@physik.uni-wuerzburg.de, giovanni.pelliccioli@physik.uni-wuerzburg.de

Abstract: Measuring the polarization of electroweak bosons at the LHC allows for important tests of the electroweak-symmetry-breaking mechanism that is realized in nature. Therefore, precise Standard Model predictions are needed for the production of polarized bosons in the presence of realistic kinematic selections. We formulate a method for the calculation of polarized cross-sections at NLO that relies on the pole approximation and the separation of polarized matrix elements at the amplitude level. In this framework, we compute NLO-accurate cross-sections for the production of two polarized Z bosons at the LHC, including for the first time NLO EW corrections and combining them with NLO QCD corrections and contributions from the gluon-induced process.

Keywords: NLO Computations

ArXiv ePrint: 2107.06579

https://doi.org/10.1007/JHEP10(2021)097

JHEP10(2021)097

Contents

JHEP10(2021)097

1 Introduction

The production of four charged leptons at the LHC provides an optimal framework to study ZZ production as well as to investigate Higgs-boson decays, both with the aim of probing the Standard Model (SM) of fundamental interactions and with the purpose of searching for new-physics effects. The presence of four charged leptons in the final state renders this signature one of the cleanest at the LHC, i.e. it features a high signal-to-background ratio, and this motivates the great interest both from the experimental and from the theoretical side in investigating this process.

Four-charged-lepton production has been measured by ATLAS and CMS with 13-TeV data to constrain the decay width of the Higgs boson [1, 2] and its anomalous couplings to SM particles [2–4]. The production of Z pairs in the four-charged-lepton channel has been employed to measure the SM cross-section [5, 6] and to constrain anomalous gauge-boson couplings [6–8]. The same channel has been used to measure the four-lepton decay of a single Z boson [5, 6]. A complete study of the full spectrum of the four-lepton invariant mass has been performed, including the measurement of single-Z and Higgs production, ZZ on-shell production and interference effects [9, 10].

The next-to-leading-order (NLO) QCD corrections to the production of Z-boson pairs have been known for almost thirty years [11–15]. The NLO electroweak (EW) corrections have been calculated for on-shell [16, 17] and for off-shell Z bosons in the four-charged-lepton channel [18, 19]. NLO EW and QCD corrections have been combined in the context of the SM [20, 21] and in the presence of anomalous couplings [22]. The next-to-next-to-leading-order (NNLO) QCD corrections to the production of four leptons have been recently

computed [23–26], and studies have been dedicated to the NLO QCD corrections to the loop-induced gluon-gluon channel [27–30]. The combination of state-of-the-art perturbative corrections has been performed, including NNLO QCD and NLO EW corrections to off-shell ZZ production [31]. The matching to a parton shower (PS) has been achieved at NLO QCD for the quark-induced [32, 33] and for the gluon-induced channel [34, 35]. Very recently the complete NLO corrections have been matched to QCD and QED PS [36], and the NNLO QCD corrections have been matched to QCD PS [37].

Thanks to the possibility of reconstructing all particles in the final state, the production of four charged leptons provides a large number of angular observables that are sensitive to the spin structure of the underlying resonances, both in the case of the Higgs and single-Z decay into four leptons, and in the case of the leptonic decay of two Z bosons. In fact, the Higgs decay into four leptons has been widely studied [38–47] and then measured with Run-2 data [1–4, 48–51] with the purpose of determining the spin and parity of the Higgs boson as well as its CP properties via angular and energy correlations.

For the process $pp \to ZZ \to e^+e^-\mu^+\mu^-$, the possibility to fully reconstruct the final state allows to access observables that are sensitive to the polarization of Z bosons. This can be done in the Higgs-resonance region [52–54], where the polarization of the weak bosons may give hints of new-physics effects in the coupling of the Higgs to longitudinally- or transversely-polarized bosons. The polarization structure can also be studied in the so-called on-shell region [17], where two Z bosons are produced and then decay into charged lepton pairs: this is the target of this paper.

The polarization of W and Z bosons has been measured at the LHC in $W + jet$ and $Z+jet$ production [55–58] and in the decay of top quarks [59–61] with Run-1 data, and more recently also in WZ production [62] and in same-sign WW scattering [63] with the 13-TeV data. The upcoming high-luminosity LHC run is expected to enhance the sensitivity to the polarization of Z bosons produced in ZZ inclusive production and scattering [64, 65].

The increasing experimental interest in measuring the weak-boson polarization in multi-boson processes has triggered a number of phenomenological studies for the LHC environment. The seminal works concerned the production of weak bosons in association with jets [66] and a number of other processes [67]. The effect of lepton cuts on polarization extraction was highlighted in refs. [66, 68]. More recently, a study of polarization-sensitive coefficients has been performed for $W^\pm Z$ inclusive production [69, 70]. The separation of polarization states at the amplitude level at leading order (LO) has been automated and investigated in vector-boson scattering [71–73] with the PHANTOM Monte Carlo [74] and in Higgs decays to four leptons [53, 54]. The generation of polarized events in general multi-boson processes is available at LO in the MadGraph framework [75] via the spin-correlated narrow-width approximation [76–78]. The separation of polarized signals at the amplitude level has been extended to NLO QCD [79, 80] and to NNLO QCD [81] for di-boson production in the fully-leptonic channel. The growing interest in the polarization structure of di-boson production and the increased sensitivity to polarization observables have motivated us to extend these polarization studies to NLO EW.

The aim of this work is twofold. On the one hand, we present a general, well-behaved definition of polarized ZZ signals (both bosons have definite polarization state) including

JHEP10(2021)097

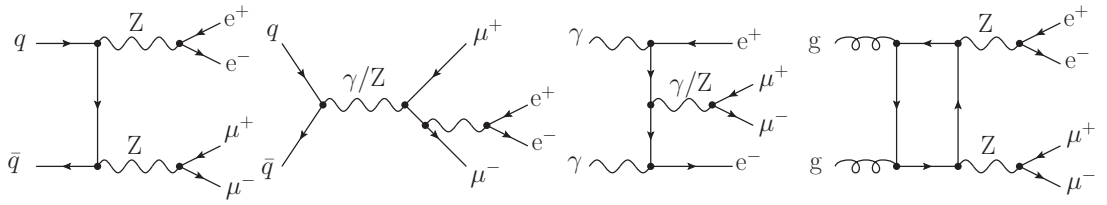

Figure 1. Sample LO Feynman diagrams for four-charged-lepton production. From left to right: ZZ-resonant diagram in the $q\bar{q}$ channel, non-doubly-resonant diagram in the $q\bar{q}$ channel, non-doubly-resonant diagram in the $\gamma\gamma$ channel, ZZ-resonant loop-induced diagram in the gg channel.

the decay modelling at NLO EW accuracy, which is achieved via the extension of the double-pole approximation (DPA) used in refs. [79, 80] to real radiation from leptonic decay products, and via the separation of polarization at the amplitude level in all parts of the calculation. On the other hand, we investigate the LHC phenomenology of polarized ZZ production including all LO and NLO contributions (both of QCD and of EW origin) in the presence of realistic kinematic selections, in order to address possible experimental analyses in this di-boson channel.

This paper is organized as follows. In section 2, we point out the main difficulties that arise when separating resonant ZZ contributions from the non-doubly-resonant ones at NLO, and we describe in detail (sections 2.1 and 2.2) our method to achieve this goal. The separation of polarizations is described in section 2.3. The SM input parameters and the kinematic setups that are used in the numerical simulations are described in sections 2.4 and 2.5, respectively. The integrated and differential results for polarized ZZ production at NLO EW are discussed in section 3.1 for an inclusive setup. The combined NLO QCD and EW corrections, as well as the loop-induced gluonic corrections to the polarization structure of ZZ production are presented in section 3.2 for a fiducial region that mimics the latest experimental selections for this process. In section 4 we draw our conclusions.

2 Calculation details

We consider the production of a ZZ pair in the fully-leptonic channel,

$$\mathrm{pp} \to \mathrm{e}^+\mathrm{e}^-\mu^+\mu^- + X\,, \tag{2.1}$$

at NLO accuracy, including both QCD and EW radiative corrections. At tree-level [$\mathcal{O}(\alpha^4)$] only quark-antiquark and photon-photon partonic channels are present, while at NLO both photon-quark and gluon-quark channels contribute to the real radiation at $\mathcal{O}(\alpha^5)$ and $\mathcal{O}(\alpha^4\alpha_\mathrm{s})$, respectively. Since the final state is charge neutral, the loop-induced gluon-gluon partonic channel [formally of order $\mathcal{O}(\alpha^4\alpha_\mathrm{s}^2)$] gives a non-negligible contribution to this process thanks to large gluon luminosity in the proton. Sample LO diagrams are shown in figure 1. Part of LO contributions to the $q\bar{q}$ and gg channels involve two Z bosons that are produced and then separately decay into charged lepton pairs: we refer to these contributions as *doubly resonant* or *ZZ resonant*. However, the full SM amplitude receives

JHEP10(2021)097

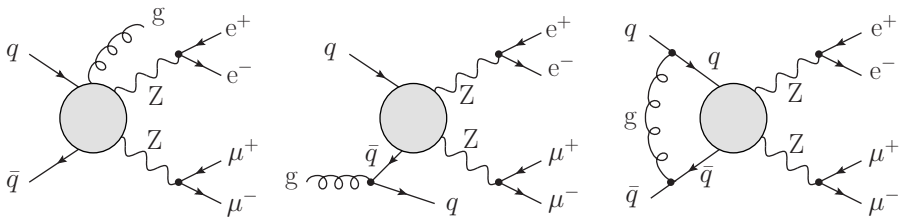

Figure 2. Sample tree-level and one-loop contributions to NLO QCD real and virtual corrections to resonant ZZ production. The shaded circle denotes arbitrary tree-level sub-diagrams.

contributions also from diagrams that do not allow for the interpretation in terms of production and decay of two Z bosons: we refer to them as *non-doubly-resonant*. In order to separate the polarization modes of Z bosons, only ZZ-resonant diagrams must be selected. Nonetheless, this selection cannot be performed simply dropping non-doubly-resonant diagrams, because the EW gauge invariance would be lost. In order to recover gauge invariance, we use a pole-approximation technique [82–87], whose details are discussed in sections 2.1 and 2.2. Another method that is often used to simulate the production and decay of unstable particles is provided by the narrow-width approximation [76–78, 81].

In the $\gamma\gamma$ partonic channel, at most one s-channel Z propagator can be present in the SM amplitude. Therefore, this partonic process cannot contribute to the ZZ-resonant production neither at LO nor at NLO EW. It contributes to the full calculation only, and we have computed it including also its complete NLO EW corrections.

The selection of ZZ-resonant diagrams and a prescription to recover gauge invariance is needed also for NLO radiative corrections of virtual and real origin. Since we consider a final state with colour-less particles, both real and virtual QCD corrections of order $\mathcal{O}(\alpha^4\alpha_s)$ only modify the structure of the initial state. This enables a simple separation between doubly-resonant and non-doubly-resonant contributions, exactly in the same fashion as at LO. Sample real and virtual diagrams for QCD corrections to resonant ZZ production are shown in figure 2. The details of the DPA used for NLO QCD corrections are described in section 2.1.

The NLO EW corrections of order $\mathcal{O}(\alpha^5)$ to the production of four charged leptons at the LHC are more involved than the QCD ones, as both real and virtual contributions modify the structure of the initial state as well as the structure of the final state, allowing for additional EW propagators (either on-shell or off-shell) connecting the initial and the final state. This non-factorized structure implies a more involved selection of ZZ-resonant diagrams, which is needed for the separation of polarization states.

Sample one-loop diagrams are shown in figure 3. In order to extract ZZ-resonant contributions, only loop diagrams that can be interpreted as production and decay of two Z bosons, called *factorizable*, must be selected. They include both corrections to the ZZ production process, like the one of figure 3(a), and corrections to the two decays $\mathrm{Z} \to \ell^+\ell^-$, $\ell = \mathrm{e}, \mu$, like the one in figure 3(b).

Also contributions with a virtual soft photon connecting either initial- and final-state particles [figure 3(c)], or two final-state particles coming from different Z-boson decays

JHEP10(2021)097

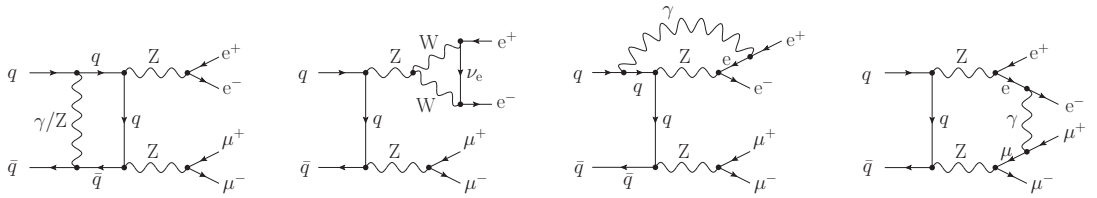

(a) Box correction to the ZZ production process

(b) Vertex correction to the decay $Z \to e^+e^-$

(c) Initial-final non-factorizable correction

(d) Final-final non-factorizable correction

Figure 3. Sample one-loop diagrams for four-charged-lepton production in the $q\bar{q}$ partonic channel at NLO EW.

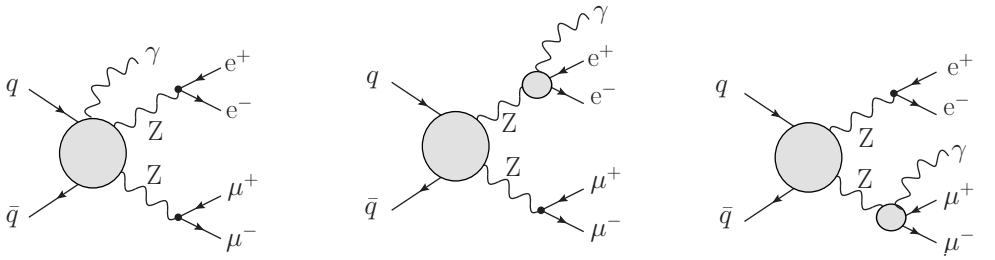

(a) Initial-state radiation (ISR)

(b) Final-state radiation from $Z \to e^+e^-$ (FSR1)

(c) Final-state radiation from $Z \to \mu^+\mu^-$ (FSR2)

Figure 4. Real-radiation contributions to resonant ZZ production in the $q\bar{q}$ partonic channel at NLO EW.

[figure 3(d)], called *non-factorizable*, are doubly resonant. In fact, such corrections are characterized by a universal structure that factorizes the doubly-resonant LO squared amplitude [88–90]. However, the impact of these corrections is expected to be small thanks to cancellations against the corresponding non-factorizable real-radiation contributions [88, 89]. Therefore, we exclude both virtual and real non-factorizable corrections from the DPA calculation.

All other one-loop, non-doubly-resonant contributions need to be dropped. The virtual EW corrections to the $\gamma\gamma$ partonic channel involve doubly-resonant contributions (box and triangle fermion-loop diagrams), which however need to be interfered with tree-level diagrams which can only be non doubly resonant. Therefore, these loop diagrams with a $\gamma\gamma$ initial state enter the DPA calculation only at order $\mathcal{O}(\alpha^6)$, in the same fashion as the gg channel gives doubly-resonant contributions at order $\mathcal{O}(\alpha^4\alpha_s^2)$.

The real-radiation contributions to resonant ZZ production in the quark-antiquark channel, shown in figure 4, can be divided in three classes. The first one concerns the radiation off the initial state [ISR, figure 4(a)], the second and the third ones are characterized by the final-state radiation (FSR1, FSR2) of a photon off the e^+e^- and $\mu^+\mu^-$ pair, respectively [see figures 4(b)–4(c)]. It is important to note that squaring the sum of real-radiation contributions as in figure 4 returns also non-factorizable corrections, arising from the interference of diagrams of different types. The soft singularities embedded in

JHEP10(2021)097

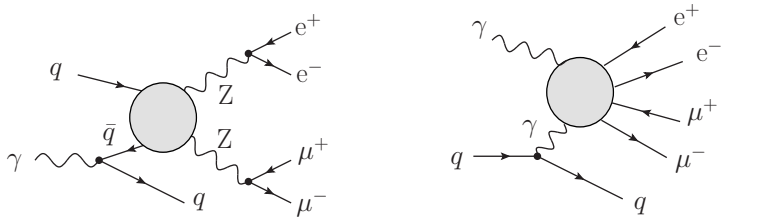

(a) ZZ-resonant contribution

(b) Non-doubly-resonant contribution

Figure 5. Real-radiation contributions to four-charged-lepton production in the γq partonic channel at NLO EW.

such contributions are cancelled by virtual non-factorizable contributions as those shown in figures 3(c)–3(d). After combining real and virtual contributions, the non-factorizable corrections are expected to be smaller than the factorizable ones, given by the incoherent sum of squared ISR, FSR1 and FSR2 corrections [88, 89].

In order to cancel infrared (IR) singularities properly, a careful selection of subtraction counterterms is needed, retaining only those (both integrated and unintegrated) that cure the singularities of doubly-resonant real corrections. In the full computation, also non-doubly-resonant structures contribute to real and virtual corrections, leading to a larger number of singular configurations that need to be subtracted. We perform the subtraction of IR divergences in the Catani-Seymour (CS) dipole formalism [91–93].

Photon-induced partonic channels open up at NLO EW. Sample diagrams for these real corrections are shown in figure 5. The selection of ZZ-resonant diagrams in this case is much easier, as the final state (anti)quark cannot come from the decay of a Z boson and the doubly-resonant contributions are of ISR type only. The diagram topologies shown in figure 5(a) and 5(b) can embed singular configurations in which the emitted (anti)quark is collinear either to the initial-state photon [figure 5(a)] or to the initial-state (anti)quark [figure 5(b)]. It is important to select only the subtraction counterterms that absorb the first kind of configurations, since the underlying LO contribution of the second configuration is non doubly resonant ($\gamma\gamma$ induced).

The selection of doubly-resonant diagrams in Born-level, virtual, and real-radiation contributions is essential to enable the separation of polarizations in Z-boson propagators. In the DPA [85, 86], the two resonant bosons must be projected on their mass shell in order to restore EW gauge invariance. This is achieved via suitable on-shell projections that are described in sections 2.1 and 2.2.

Before going into the details of the DPA used for this calculation, we point out that the neutral electric charge of the Z boson simplifies the selection of doubly-resonant structures both in real and in virtual corrections, as photons cannot be radiated off the resonant Z-bosons. In the case of W bosons, additional care must be taken in the separation of initial-state and final-state radiation contributions, in particular concerning the definition of subtraction counterterms. We postpone the treatment of charged resonances at NLO EW to future work.

JHEP10(2021)097

2.1 A double-pole approximation for Born-like doubly-resonant structures

After selecting doubly-resonant diagrams, it is crucial to apply an on-shell projection to all LO and NLO matrix elements for ZZ production, retaining the off-shell-ness of the Breit-Wigner modulation in the denominator of Z-boson propagators. This has to be pursued with special attention to the subtraction counterterms, devising suitable projections that do not spoil the cancellation of IR singularities. A general NLO (either QCD or EW) observable receives the following contributions in the dipole formalism [91–93],

$$\begin{aligned}\left(\frac{\mathrm{d}\sigma}{\mathrm{d}\xi}\right)_{\mathrm{NLO}} = {} & \frac{1}{2s}\int \mathrm{d}\Phi_n^{(4)}\ \mathcal{B}(\Phi_n^{(4)})\,\delta(\xi-\xi_n) \\ & + \frac{1}{2s}\int \mathrm{d}\Phi_n^{(4)}\left[\mathcal{V}(\Phi_n^{(D)}) + \mathcal{C}(\Phi_n^{(D)}) + \int \mathrm{d}\Phi_{\mathrm{rad}}^{(D)}\ \mathcal{D}(\Phi_n^{(D)},\Phi_{\mathrm{rad}}^{(D)})\right]_{D=4}\delta(\xi-\xi_n) \\ & + \frac{1}{2s}\int \mathrm{d}\Phi_{n+1}^{(4)}\ \left[\mathcal{R}(\Phi_{n+1}^{(4)})\,\delta(\xi-\xi_{n+1}) - \mathcal{D}(\bar{\Phi}_n^{(4)},\Phi_{\mathrm{rad}}^{(4)})\,\delta(\xi-\xi_n)\right], \end{aligned} \tag{2.2}$$

where $\mathcal{B}$, $\mathcal{V}$, $\mathcal{R}$ are Born, virtual and real squared matrix elements, respectively, including spin and colour averages as well as symmetry factors, while $1/(2s)$ is the flux factor. The $\mathcal{D}$ term is the sum of subtraction dipoles that appears both in its 4-dimensional, unintegrated version and in its D-dimensional, integrated version. The quantity $\mathcal{C}$ represents the collinear counterterm that cancels left-over collinear singularities of initial-state type. The arguments of the δ symbols indicate whether the observable ξ is evaluated with n-body or with $(n+1)$-body kinematics (with $D=4$). Note that the subtraction dipoles depend on the mapped n-body kinematics $\bar{\Phi}_n$, which is derived from $(n+1)$-body kinematics via CS mappings [91], and on the radiation phase-space measure Φ_{rad}. While we keep n variable in the formulas, $n=4$ for ZZ production with leptonic Z decays.

Let us consider all NLO contributions which embed a doubly-resonant sub-amplitude with two two-body decays, namely $\mathrm{Z}(\to \mathrm{e}^+\mathrm{e}^-)\,\mathrm{Z}(\to \mu^+\mu^-)$. This is the case for Born matrix elements, virtual corrections, integrated dipoles, and real-subtracted initial-state radiation contributions.

We label the pole approximation applied to these contributions with $\mathrm{DPA}^{(2,2)}$. Let us call q_1, q_2 the two off-shell Z-boson momenta in the laboratory system, and $\tilde{q}_1, \tilde{q}_2$ the corresponding on-shell-projected momenta. We choose $\tilde{q}_1, \tilde{q}_2$ such that

$$\tilde{q}_1 + \tilde{q}_2 = q_1 + q_2, \qquad \tilde{q}_1^2 = \tilde{q}_1^2 = M_{\mathrm{Z}}^2 \tag{2.3}$$

and the spatial direction of the two bosons in the di-boson centre-of-mass frame is preserved [86]. This procedure is valid for $M_{\mathrm{e}^+\mathrm{e}^-\mu^+\mu^-} > 2M_{\mathrm{Z}}$. In the four-charged-lepton channel, this constraint can be achieved also experimentally thanks to the reconstructable final state [10].

We are left with the modification of the momenta of the four final-state leptons, according to the on-shell kinematics of the two projected bosons. Considering the $\mathrm{Z}(q_1) \to \mathrm{e}^+(k_1)\,\mathrm{e}^-(k_2)$ decay, we choose to preserve the energy fraction and the spatial direction of the electron (and of the positron) in the corresponding Z rest frame:

– we boost k_1, k_2 into the rest frame of the off-shell Z boson (momentum q_1), where the two lepton momenta have $\hat{n}_{k_1}$ and $\hat{n}_{k_2}$ as spatial directions;

JHEP10(2021)097

– we rescale the lepton energies according to the on-shell-ness of the projected Z boson, i.e. we multiply the off-shell energies by $M_{\mathrm{Z}}/\sqrt{q_1^2}$;

– we set the spatial directions in the rest frame of the on-shell Z bosons equal to the off-shell ones ($\hat{n}_{k_1}$, $\hat{n}_{k_2}$); it is easy to see that in this reference frame the two projected momenta of the leptons read $\tilde{k}_1 = (1, \hat{n}_{k_1})M_{\mathrm{Z}}/2$ and $\tilde{k}_2 = (1, -\hat{n}_{k_1})M_{\mathrm{Z}}/2$;

– we boost back $\tilde{k}_1, \tilde{k}_2$ into the laboratory frame according to the projected Z-boson kinematics (momentum $\tilde{q}_1$).

The same procedure is then applied to the decay products of the second Z boson ($\mathrm{Z} \to \mu^+\mu^-$).

The described DPA can be safely applied to factorizable virtual corrections and integrated dipoles, as well as to the real-subtracted corrections of ISR type. Since the QCD corrections only modify the ZZ production process, all contributions at order $\mathcal{O}(\alpha^4\alpha_{\mathrm{s}})$ can be treated with DPA$^{(2,2)}$. Note that only two subtraction dipoles are needed to cancel IR singularities of QCD origin, and they are both of initial-initial type, therefore the modification of the momenta of final-state leptons (colourless) does not interfere with the phase-space mappings used in subtraction counterterms. Both subtraction terms $\mathcal{D}$ and initial-state collinear counterterms $\mathcal{C}$ [in eq. (2.2)] need to be computed with DPA$^{(2,2)}$. This DPA has already been used to compute NLO QCD corrections to polarized $\mathrm{W}^+\mathrm{W}^-$ and $\mathrm{W}^+\mathrm{Z}$ production [79, 80].

In the computation of real EW corrections, only ISR contributions [see figure 4(a)] can be computed with DPA$^{(2,2)}$, following the same procedure that has been used in the NLO QCD case, but taking care of one additional subtlety. Differently from QCD corrections, the spectator for the ISR subtraction dipoles may be an initial-state or a final-state particle. However, only an initial-state spectator must be selected to properly cancel the IR singularities of ISR type only in DPA$^{(2,2)}$. Furthermore, treating the $(n+1)$-body kinematics and the mapped kinematics (in the sense of CS mappings) with the same DPA technique ensures that the subtraction is not spoiled. Adapting the notation of eq. (2.2), the real-subtracted contribution reads (with off-shell kinematics),

$$\mathcal{R}_{\mathrm{ISR}}(\Phi_{n+1})\,\delta(\xi-\xi_{n+1}) - \mathcal{D}^{I_1 i, I_2}(\bar{\Phi}_n, \Phi_{\mathrm{rad}}(k_i))\,\delta(\xi-\xi_n) - \mathcal{D}^{I_2 i, I_1}(\bar{\Phi}_n, \Phi_{\mathrm{rad}}(k_i))\,\delta(\xi-\xi_n)\,, \tag{2.4}$$

where $\bar{\Phi}_n$ is the mapped n-body kinematics, according to an initial-initial CS mapping, while k_i is the radiated-photon momentum. Both the emitter and the spectator are initial-state particles (I_1, I_2). After the application of DPA$^{(2,2)}$,

$$\mathcal{R}_{\mathrm{ISR}}(\tilde{\Phi}_{n+1})\,\delta(\xi-\xi_{n+1}) - \mathcal{D}^{I_1 i, I_2}(\tilde{\bar{\Phi}}_n, \Phi_{\mathrm{rad}}(k_i))\,\delta(\xi-\xi_n) - \mathcal{D}^{I_2 i, I_1}(\tilde{\bar{\Phi}}_n, \Phi_{\mathrm{rad}}(k_i))\,\delta(\xi-\xi_n)\,, \tag{2.5}$$

where $\tilde{\bar{\Phi}}_n$ and $\tilde{\Phi}_{n+1}$ represent the on-shell-projected momenta of the n- and $(n+1)$-body phase space. The DPA$^{(2,2)}$ does not modify the photon radiation, neither in the $(n+1)$-body kinematics, nor in the radiation phase-space that appears in the dipoles. Since the initial-initial CS mappings modify all final-state particles with the same boost, the application of DPA$^{(2,2)}$ to the mapped kinematics does not interfere with the CS-mapping procedure, as

JHEP10(2021)097

the total momentum of the four leptons is preserved in the DPA, i.e. the on-shell projection of DPA$^{(2,2)}$ and the initial-initial CS mappings commute.

Note that the DPA$^{(2,2)}$ can also be used to treat the photon-induced real contributions, since the corresponding doubly-resonant contributions do not allow for final-state radiation.

We stress that, since also integrated dipoles are treated with DPA$^{(2,2)}$, the needed correspondence between subtraction and integrated dipoles is maintained for ISR contributions.

2.2 A double-pole approximation for final-state radiation

The treatment of final-state-radiation contributions to EW real corrections is more delicate than the treatment of ISR ones. Let us consider the case in which a Z boson decays into $\mathrm{e}^+(k_1)\,\mathrm{e}^-(k_2)\,\gamma(k_5)$, while the other one decays into $\mu^+(k_3)\,\mu^-(k_4)$, corresponding to the diagram topology shown in figure 4(b). For such corrections, we have devised an on-shell projection (labelled DPA$^{(3,2)}$) that differs from DPA$^{(2,2)}$ but follows the same driving idea in terms of preserved quantities. For the projection of the momenta of Z bosons, we apply the same method as for DPA$^{(2,2)}$, with the difference that the momentum of the first Z boson is now given by the sum of three momenta,

$$q_1 = k_1 + k_2 + k_5, \qquad q_2 = k_3 + k_4\,. \tag{2.6}$$

After this step, we have $\tilde{q}_1^2 = \tilde{q}_2^2 = M_\mathrm{Z}^2$ and $\tilde{q}_1 + \tilde{q}_2 = q_1 + q_2$. The momenta k_3, k_4 can be projected following the prescription of DPA$^{(2,2)}$ (see section 2.1), as a two-body decay is understood for the second Z boson. For the three-body decay,

- we boost k_1, k_2, k_5 into the rest frame of the off-shell Z boson (momentum q_1), where the three particles have $\hat{n}_{k_1}, \hat{n}_{k_2}, \hat{n}_{k_5}$ as spatial directions;
- we rescale the lepton and photon energies according to the on-shell-ness of the projected Z boson, i.e. we multiply the off-shell energies by $M_\mathrm{Z}/\sqrt{q_1^2}$;
- we set the spatial directions of the final-state momenta in the rest frame of the on-shell Z boson equal to the off-shell ones ($\hat{n}_{k_1}$, $\hat{n}_{k_2}$, $\hat{n}_{k_5}$), which allows to preserve the relative angles among the three particles;
- we boost back $\tilde{k}_1, \tilde{k}_2, \tilde{k}_5$ into the laboratory frame according to the projected Z-boson kinematics (momentum $\tilde{q}_1$).

It is easy to check that this prescription does not violate momentum-conservation and preserves the ratio of Lorentz invariants constructed with the three decay products,

$$\frac{\tilde{k}_a \cdot \tilde{k}_b}{\tilde{k}_a \cdot \tilde{k}_c} = \frac{k_a \cdot k_b}{k_a \cdot k_c} \quad \text{for any} \quad a, b, c = 1, 2, 5 \;\text{ and }\; a \neq b \neq c\,. \tag{2.7}$$

It is crucial that the energy fractions and the relative angles are preserved in the three-body decay, as the radiated photon may be soft and/or collinear to the electron or to the positron. The DPA$^{(3,2)}$ guarantees that the soft-ness and/or collinearity of the photon is preserved.

JHEP10(2021)097

The subtracted FSR1 real corrections read [with off-shell $(n+1)$-body kinematics]:

$$\mathcal{R}_{\mathrm{FSR1}}(\Phi_{n+1})\,\delta(\xi-\xi_{n+1}) - \mathcal{D}^{15,2}(\bar{\Phi}_n,\Phi_{\mathrm{rad}}(k_5))\,\delta(\xi-\xi_n) - \mathcal{D}^{25,1}(\bar{\Phi}_n,\Phi_{\mathrm{rad}}(k_5))\,\delta(\xi-\xi_n)\,, \tag{2.8}$$

where $\bar{\Phi}_n$ is the mapped phase-space according to a final-final CS mapping. The contributing dipoles involve as emitter and spectator either the electron or the positron, which form with the photon the decay products of the first Z boson. At variance with the DPA$^{(2,2)}$, the photon momentum k_5 is modified by the DPA$^{(3,2)}$. Therefore the same DPA must be applied to the radiation phase-space and to the factorized phase-space in the CS-mapped process to guarantee the proper subtraction of IR singularities. This could spoil the correspondence between the subtraction dipoles appearing in eq. (2.8) and their integrated counterparts, as the former are projected with DPA$^{(3,2)}$, while the latter can only be projected with DPA$^{(2,2)}$ (as they feature n-body kinematics). We will see in the following that this is not the case.

If no DPA is applied, the CS mapping for $\mathcal{D}^{15,2}$ reads,

$$\bar{k}_1 = k_1 + k_5 - \frac{s_{15}}{s_{12}+s_{25}}\,k_2\,, \quad \bar{k}_2 = \frac{s_{125}}{s_{12}+s_{25}}\,k_2\,, \quad \bar{k}_3 = k_3\,, \quad \bar{k}_4 = k_4\,, \tag{2.9}$$

where $s_{ab} = 2k_a\cdot k_b$ and $s_{125} = s_{12}+s_{25}+s_{15}$. In order to use the DPA for the subtraction dipoles, we cannot simply apply the DPA$^{(2,2)}$ to the mapped momenta, otherwise we would implicitly assume that the photon momentum is untouched, which is not the case when applying DPA$^{(3,2)}$ to FSR1 real contributions. A consistent procedure is to apply the CS mapping to the $(n+1)$-body kinematics that has already been projected with the DPA$^{(3,2)}$,

$$\bar{\tilde{k}}_1 = \tilde{k}_1 + \tilde{k}_5 - \frac{\tilde{s}_{15}}{\tilde{s}_{12}+\tilde{s}_{25}}\,\tilde{k}_2\,, \quad \bar{\tilde{k}}_2 = \frac{\tilde{s}_{125}}{\tilde{s}_{12}+\tilde{s}_{25}}\,\tilde{k}_2\,, \quad \bar{\tilde{k}}_3 = \tilde{k}_3\,, \quad \bar{\tilde{k}}_4 = \tilde{k}_4\,. \tag{2.10}$$

The final-final CS mapping does not modify the virtuality of the Z boson [$\tilde{q}_1^2 = (\tilde{k}_1+\tilde{k}_2+\tilde{k}_5)^2 = M_{\mathrm{Z}}^2$]. Furthermore, according to eq. (2.7), the Lorentz invariants that appear in eq. (2.10) coincide with those of eq. (2.9).

The more involved character of the DPA$^{(3,2)}$ with respect to DPA$^{(2,2)}$ originates from the fact that the on-shell projection of DPA$^{(3,2)}$ and the final-final CS mappings are not commuting, unlike the case of DPA$^{(2,2)}$ application and initial-initial CS mappings. In order to further prove the decent behaviour of the DPA$^{(3,2)}$, we check that its application to the subtracted final-state-radiation corrections does not spoil the correspondence between unintegrated and integrated dipoles. Let us consider the D-dimensional structure of a dipole with emissus i (photon), emitter j (e^+ or e^-) and spectator k (e^- or e^+), recalling that the three particles are decay products of the same Z resonance,

$$\begin{aligned}
&\mathrm{d}\bar{\Phi}_n\,\mathrm{d}\Phi_{\mathrm{rad}}(k_i)\,\mathcal{D}^{(ji,k)}(\bar{\Phi}_n,\Phi_{\mathrm{rad}}(k_i)) \\
&\quad = \mathrm{d}\bar{\Phi}_n\,\mathrm{d}y\,\mathrm{d}z\,\frac{(\bar{s}_{jk})^{-\epsilon}}{16\pi^2}\,\frac{(4\pi)^\epsilon}{\Gamma(1-\epsilon)}\,[z\,(1-z)]^{-\epsilon}(1-y)^{1-2\epsilon}y^{-1-\epsilon} \\
&\qquad\quad \times\left(-\frac{Q_j\,Q_k}{Q_j^2}\right)\langle\bar{k}_1,\dots,\bar{k}_n|\,V_{ijk}\,|\bar{k}_1,\dots,\bar{k}_n\rangle\,\mathcal{B}(\bar{\Phi}_n),
\end{aligned} \tag{2.11}$$

JHEP10(2021)097

where Q_j, Q_k are the electric charges (in unit of e) of the emitter and spectator, respectively, and the phase-space measure depends on the variables

$$y = \frac{s_{ij}}{s_{ijk}} = \left(1 + \frac{s_{jk}}{s_{ij}} + \frac{s_{ik}}{s_{ij}}\right)^{-1}, \qquad z = \frac{s_{ik}}{s_{ijk} - s_{ij}} = \left(1 + \frac{s_{jk}}{s_{ik}}\right)^{-1}. \tag{2.12}$$

The kernel that has to be integrated is [91, 92]

$$\langle s|V_{ijk}(y,z)|s'\rangle \;=\; 8\pi\alpha\,\mu^{2\epsilon}\,Q_j^2\left(\frac{2}{1-z(1-y)} - (1+z) - \epsilon\,(1-z)\right)\delta_{ss'}\,. \tag{2.13}$$

We can then re-write eq. (2.11) as

$$\begin{aligned}
&\mathrm{d}\bar{\Phi}_n\,\mathrm{d}\Phi_{\mathrm{rad}}(k_i)\,\mathcal{D}^{(ji,k)}(\bar{\Phi}_n,\Phi_{\mathrm{rad}}(k_i)) \\
&\quad= \mathrm{d}\bar{\Phi}_n\,\frac{\alpha}{2\pi}\,\frac{(4\pi)^\epsilon}{\Gamma(1-\epsilon)}\left(\frac{\mu^2}{\bar{s}_{jk}}\right)^{\epsilon}\mathcal{B}(\bar{\Phi}_n) \\
&\qquad\qquad\times\;\mathrm{d}y\,\mathrm{d}z\,[z\,(1-z)]^{-\epsilon}(1-y)^{1-2\epsilon}y^{-1-\epsilon}\left(\frac{2}{1-z(1-y)} - (1+z) - \epsilon\,(1-z)\right),
\end{aligned}$$

where we have used $Q_jQ_k = -1$ and $Q_j^2 = 1$ for the $\mathrm{e}^+\mathrm{e}^-$ final state. The 4-dimensional version of the subtraction dipole reads

$$\mathrm{d}\bar{\Phi}_n\,\frac{\alpha}{2\pi}\;\mathcal{B}(\bar{\Phi}_n)\;\mathrm{d}y\,\mathrm{d}z\,\frac{1-y}{y}\left(\frac{2}{1-z(1-y)} - (1+z)\right), \tag{2.14}$$

while its integration in D dimensions ($D = 4-2\epsilon$) gives

$$\mathrm{d}\bar{\Phi}_n\,\frac{\alpha}{2\pi}\,\frac{(4\pi)^\epsilon}{\Gamma(1-\epsilon)}\left(\frac{\mu^2}{\bar{s}_{jk}}\right)^{\epsilon}\left[\frac{1}{\epsilon^2} + \frac{3}{2\epsilon} + \left(5 - \frac{\pi^2}{2}\right) + \mathcal{O}(\epsilon)\right]\mathcal{B}(\bar{\Phi}_n)\,. \tag{2.15}$$

For ZZ production, we have $n = 4$ and the LO doubly-resonant structure can be written as

$$\mathcal{B}\Big(\bar{k}_1^{(j5,k)},\bar{k}_2^{(j5,k)},\bar{k}_3^{(j5,k)},\bar{k}_4^{(j5,k)}\Big) = \frac{\mathcal{N}_{\mathcal{B}}\left(\bar{k}_1^{(j5,k)},\bar{k}_2^{(j5,k)},\bar{k}_3^{(j5,k)},\bar{k}_4^{(j5,k)}\right)}{\left[\left(\bar{s}_{12}^{(j5,k)} - M_{\mathrm{Z}}^2\right)^2 + (\Gamma_{\mathrm{Z}}M_{\mathrm{Z}})^2\right]\left[\left(\bar{s}_{34}^{(j5,k)} - M_{\mathrm{Z}}^2\right)^2 + (\Gamma_{\mathrm{Z}}M_{\mathrm{Z}})^2\right]}, \tag{2.16}$$

where the barred kinematics depends on the choice of the emitter j and spectator k that is used in the dipole phase-space mapping. The mapped momenta are labelled by the indices of the emitter-emissus pair $j5$ and the spectator k. The $(n+1)$-body part of the NLO correction for the doubly-resonant FSR1 contribution reads (k_5 is the photon momentum):

$$\begin{aligned}
&\mathrm{d}\Phi_{n+1}\,\frac{\mathcal{N}_{\mathcal{R}}(k_1,k_2,k_3,k_4,k_5)}{\left[\left(s_{125} - M_{\mathrm{Z}}^2\right)^2 + (\Gamma_{\mathrm{Z}}M_{\mathrm{Z}})^2\right]\left[\left(s_{34} - M_{\mathrm{Z}}^2\right)^2 + (\Gamma_{\mathrm{Z}}M_{\mathrm{Z}})^2\right]}\,\delta(\xi - \xi_{n+1}) \\
&\quad- \mathrm{d}\bar{\Phi}_n^{(15,2)}\,\frac{\alpha}{2\pi}\,\frac{\mathcal{N}_{\mathcal{B}}(\bar{k}_1^{(15,2)},\bar{k}_2^{(15,2)},\bar{k}_3^{(15,2)},\bar{k}_4^{(15,2)})}{\left[\left(\bar{s}_{12}^{(15,2)} - M_{\mathrm{Z}}^2\right)^2 + (\Gamma_{\mathrm{Z}}M_{\mathrm{Z}})^2\right]\left[\left(\bar{s}_{34}^{(15,2)} - M_{\mathrm{Z}}^2\right)^2 + (\Gamma_{\mathrm{Z}}M_{\mathrm{Z}})^2\right]} \\
&\qquad\times\;\mathrm{d}y\,\mathrm{d}z\,\frac{1-y}{y}\left(\frac{2}{1-z(1-y)} - (1+z)\right)\delta(\xi - \xi_n) \\
&\quad- \mathrm{d}\bar{\Phi}_n^{(25,1)}\,\frac{\alpha}{2\pi}\,\frac{\mathcal{N}_{\mathcal{B}}(\bar{k}_1^{(25,1)},\bar{k}_2^{(25,1)},\bar{k}_3^{(25,1)},\bar{k}_4^{(25,1)})}{\left[\left(\bar{s}_{12}^{(25,1)} - M_{\mathrm{Z}}^2\right)^2 + (\Gamma_{\mathrm{Z}}M_{\mathrm{Z}})^2\right]\left[\left(\bar{s}_{34}^{(25,1)} - M_{\mathrm{Z}}^2\right)^2 + (\Gamma_{\mathrm{Z}}M_{\mathrm{Z}})^2\right]} \\
&\qquad\times\;\mathrm{d}y'\,\mathrm{d}z'\,\frac{1-y'}{y'}\left(\frac{2}{1-z'(1-y')} - (1+z')\right)\delta(\xi - \xi_n)\,,
\end{aligned} \tag{2.17}$$

JHEP10(2021)097

where y', z' are defined as y, z up to the exchange of the momenta k_1 and k_2. Note also that, according to the final-final CS mapping, $\bar{s}^{(15,2)} = \bar{s}^{(25,1)} = s_{125}$ and $\bar{s}_{34}^{(15,2)} = \bar{s}_{34}^{(25,1)} = s_{34}$.

We observe that the action of $\mathrm{DPA}^{(2,2)}$ on the mapped n-body kinematics would result in the modification of the radiation measure $\mathrm{d}\Phi_{\mathrm{rad}}(k_i)$ as well as of the subtraction dipole, because the radiation momentum would be left untouched by the on-shell projection. On the contrary, if $\mathrm{DPA}^{(3,2)}$ is applied to the factorized $(n+1)$-body kinematics, both the integration measure and the dipoles do not change thanks to eq. (2.7). Furthermore, this way the three partons are correctly projected to reconstruct an on-shell Z boson. The application of $\mathrm{DPA}^{(3,2)}$ to both the complete and the factorized $(n+1)$-body kinematics gives the DPA-regulated version of eq. (2.17):

$$
\begin{aligned}
\mathrm{d}\Phi_{n+1} & \frac{\mathcal{N}_{\mathcal{R}}(\tilde{k}_1, \tilde{k}_2, \tilde{k}_3, \tilde{k}_4, \tilde{k}_5)}{\left[(s_{125} - M_{\mathrm{Z}}^2)^2 + (\Gamma_{\mathrm{Z}} M_{\mathrm{Z}})^2\right]\left[(s_{34} - M_{\mathrm{Z}}^2)^2 + (\Gamma_{\mathrm{Z}} M_{\mathrm{Z}})^2\right]}\, \delta(\xi - \xi_{n+1}) \\
& - \mathrm{d}\bar{\Phi}_n^{(15,2)}\, \frac{\alpha}{2\pi}\, \frac{\mathcal{N}_{\mathcal{B}}(\bar{\tilde{k}}_1^{(15,2)}, \bar{\tilde{k}}_2^{(15,2)}, \bar{\tilde{k}}_3^{(15,2)}, \bar{\tilde{k}}_4^{(15,2)})}{\left[(s_{125} - M_{\mathrm{Z}}^2)^2 + (\Gamma_{\mathrm{Z}} M_{\mathrm{Z}})^2\right]\left[(s_{34} - M_{\mathrm{Z}}^2)^2 + (\Gamma_{\mathrm{Z}} M_{\mathrm{Z}})^2\right]} \\
& \qquad \times \mathrm{d}y\, \mathrm{d}z\, \frac{1-y}{y} \left(\frac{2}{1 - z(1-y)} - (1+z)\right) \delta(\xi - \xi_n) \\
& - \mathrm{d}\bar{\Phi}_n^{(25,1)}\, \frac{\alpha}{2\pi}\, \frac{\mathcal{N}_{\mathcal{B}}(\bar{\tilde{k}}_1^{(25,1)}, \bar{\tilde{k}}_2^{(25,1)}, \bar{\tilde{k}}_3^{(25,1)}, \bar{\tilde{k}}_4^{(25,1)})}{\left[(s_{125} - M_{\mathrm{Z}}^2)^2 + (\Gamma_{\mathrm{Z}} M_{\mathrm{Z}})^2\right]\left[(s_{34} - M_{\mathrm{Z}}^2)^2 + (\Gamma_{\mathrm{Z}} M_{\mathrm{Z}})^2\right]} \\
& \qquad \times \mathrm{d}y'\, \mathrm{d}z'\, \frac{1-y'}{y'} \left(\frac{2}{1 - z'(1-y')} - (1+z')\right) \delta(\xi - \xi_n)\,,
\end{aligned}
\tag{2.18}
$$

where we have used the fact that $\tilde{y} = y$ and $\tilde{z} = z$, since these variables only depend on ratios of $(n+1)$-body invariants that are preserved according to eq. (2.7). We stress again that the momenta in the numerators $\mathcal{N}_{\mathcal{B}}$ are obtained from $(n+1)$-body kinematics performing first the DPA and then the CS mapping (the procedures do not commute). Owing to eq. (2.7) the integration measure $\mathrm{d}y\, \mathrm{d}z$ is left untouched by the DPA, and the integrated dipoles do not need to be modified but give exactly the expression of eq. (2.15). This is the case because the $\mathrm{DPA}^{(2,2)}$ applied to the n-body kinematics of the integrated dipoles proceeds in the same fashion as $\mathrm{DPA}^{(3,2)}$.

The analogous procedure, which we label $\mathrm{DPA}^{(2,3)}$, is applied to FSR2 real contributions shown in figure 4(c) and the corresponding two subtraction dipoles.

The entire DPA formalism that we have presented for ZZ inclusive production, in particular the on-shell projections for Born-like and final-state radiation structures, can be straightforwardly extended to more complicated processes involving Z bosons, e.g. ZZ scattering, or other neutral resonances.

As a last comment of this section, we stress that the DPA can be applied rather straightforwardly to same-flavour leptonic decays, e.g. $\mathrm{pp} \to \mathrm{Z}(\mathrm{e}^+\mathrm{e}^-)\mathrm{Z}(\mathrm{e}^+\mathrm{e}^-) + X$. The intrinsic ambiguity in identifying the resonances can be solved by associating the identical final-state leptons to specific Z bosons and accounting for the proper symmetry factor in the resonant amplitudes. A DPA for a process with such an ambiguity has, for instance, been used in ref. [94] (see discussion in section 2.2 there).

JHEP10(2021)097

2.3 Separating polarizations

The application of the DPA to all contributions of the NLO (EW or QCD) computation enables us to isolate in a gauge-invariant way the resonant contributions to ZZ production from the non-doubly-resonant background, which can be estimated as the difference between the full result and the doubly-resonant contributions in the DPA, and is expected to amount to $\mathcal{O}(\Gamma_Z/M_Z) \approx 2.7\%$ of the full result.

Thanks to the DPA, it is possible to separate the polarization of Z bosons at the level of doubly-resonant amplitudes, following the procedure that has already been applied to vector-boson scattering [71–73], to W^+Z and W^+W^- production at NLO QCD [79, 80], and to Higgs decays [53, 54]. After selecting doubly-resonant diagrams, the following structure (written in the 't Hooft-Feynman gauge) characterizes the SM amplitude,

$$\mathcal{A}_{\text{res}} = \mathcal{P}_{\mu\nu}(q_1, q_2)\, \frac{-g^{\mu\alpha}}{q_1^2 - M_Z^2 + i\Gamma_Z M_Z}\, \frac{-g^{\nu\beta}}{q_2^2 - M_Z^2 + i\Gamma_Z M_Z}\, \mathcal{D}_\alpha^{(1)}(q_1)\, \mathcal{D}_\beta^{(2)}(q_2)\,, \tag{2.19}$$

where $\mathcal{P}$ is the production part of the amplitude, while the $\mathcal{D}$ terms (not to be confused with the subtraction terms in sections 2.1 and 2.2) are the parts corresponding to the two- or three-body decays of the Z bosons. Writing the metric tensors in terms of polarization vectors, eq. (2.19) becomes

$$\begin{aligned}
\mathcal{A}_{\text{res}} &= \mathcal{P}_{\mu\nu}(q_1, q_2)\, \frac{\left[\sum_{\lambda=\text{L},\pm} \varepsilon_\lambda^{\mu\,*}(q_1)\, \varepsilon_\lambda^{\alpha}(q_1)\right] - q_1^\mu q_1^\alpha / M_Z^2}{q_1^2 - M_Z^2 + i\Gamma_Z M_Z}\, \mathcal{D}_\alpha^{(1)}(q_1) \\
&\qquad \times \frac{\left[\sum_{\lambda'=\text{L},\pm} \varepsilon_{\lambda'}^{\nu\,*}(q_2)\, \varepsilon_{\lambda'}^{\beta}(q_2)\right] - q_2^\nu q_2^\beta / M_Z^2}{q_2^2 - M_Z^2 + i\Gamma_Z M_Z}\, \mathcal{D}_\beta^{(2)}(q_2) \\
&= \sum_{\lambda=\text{L},\pm} \sum_{\lambda'=\text{L},\pm} \left[\mathcal{P}_{\mu\nu}(q_1, q_2)\, \varepsilon_\lambda^{\mu\,*}(q_1) \varepsilon_{\lambda'}^{\nu\,*}(q_2)\right] \frac{\left[\varepsilon_\lambda^{\alpha}(q_1)\, \mathcal{D}_\alpha^{(1)}(q_1)\right]}{q_1^2 - M_Z^2 + i\Gamma_Z M_Z}\, \frac{\left[\varepsilon_{\lambda'}^{\beta}(q_2)\, \mathcal{D}_\beta^{(2)}(q_2)\right]}{q_2^2 - M_Z^2 + i\Gamma_Z M_Z} \\
&\equiv \sum_{\lambda=\text{L},\pm} \sum_{\lambda'=\text{L},\pm} \mathcal{A}_{\lambda\lambda'}\,,
\end{aligned} \tag{2.20}$$

where for both Z bosons the polarization sum runs over the longitudinal (L), left-handed (−), and right-handed states (+). Since we consider massless final-state leptons, the gauge terms that are proportional to the boson momenta vanish for all LO and NLO contributions. In fact, it is easy to see that the Z-boson propagators are always contracted with massless fermionic currents, both in tree-level and in one-loop doubly-resonant amplitudes. In the general case, the contributions of the terms proportional to boson momenta in the Z-boson propagators cancel against diagrams where the Z bosons are replaced by the corresponding would-be Goldstone bosons.

From eq. (2.20) it is clear that applying the DPA and squaring the doubly-resonant (unpolarized) amplitude, one obtains well-defined polarized squared matrix elements and off-diagonal contributions which are called interference terms:

$$|\mathcal{A}_{\text{res}}|^2 = \sum_{\lambda=\text{L},\pm} \sum_{\lambda'=\text{L},\pm} |\mathcal{A}_{\lambda\lambda'}|^2 + (\text{interference terms})\,. \tag{2.21}$$

JHEP10(2021)097

Replacing the unpolarized squared matrix element with a single $\{\lambda, \lambda'\}$ term in the sum of eq. (2.21), we can generate events for the production and decay of two Z bosons with definite polarization states (λ and λ', respectively).

In order to reduce the number of different contributions and to minimize the impact of interference terms, we have defined the transverse mode (T) as the coherent sum of the left- and right-handed modes (including the left-right interference).

The polarization vectors in eq. (2.20) must be defined in a certain reference frame. Common choices for di-boson production are the laboratory (LAB) frame [69, 79] and the centre-of-mass (CM) frame of the two bosons [70, 80]. The CM-frame choice has been shown [80] to be more natural than the LAB one for di-boson production and has been used in the latest ATLAS analysis of $W^{\pm}Z$ production [62]. It is essential that the same definition of polarization vectors is used in all parts of the NLO calculation. In the case of the CM-frame definition, for final-state-radiation contributions to NLO EW corrections, the CM frame is the rest frame of the system formed by the four charged leptons and the photon, which is crucial to have a functioning subtraction of IR singularities. In section 3.1 we compare the results in both the CM- and the LAB-frame definitions, while in section 3.2 we only consider polarizations defined in the CM frame.

Before presenting the numerical results of our calculation, it is worth recalling that the polarization structure of ZZ production at the LHC is expected to be rather different from the one of W^+W^- [79, 81], in spite of the same contributing partonic channels. At LO, the differential cross-sections for on-shell ZZ production in $q\bar{q}$ annihilation can be written in terms of the CM energy squared s and the scattering angle θ in the CM frame,

$$
\begin{aligned}
\frac{\mathrm{d}\sigma_{\mathrm{LL}}}{\mathrm{d}\cos\theta} &= \frac{\pi\alpha^2(c_{\mathrm{L,q}}^4+c_{\mathrm{R,q}}^4)}{192\,s_{\mathrm{w}}^4\,c_{\mathrm{w}}^4}\,\frac{2M_{\mathrm{Z}}^4\left(s-4M_{\mathrm{Z}}^2\right)\sin^2\theta\cos^2\theta}{\sqrt{1-(4M_{\mathrm{Z}}^2/s)}\left(s\,(4M_{\mathrm{Z}}^2-s)\,\cos^2\theta+(s-2M_{\mathrm{Z}}^2)^2\right)^2} \\
&= \frac{\pi\alpha^2(c_{\mathrm{L,q}}^4+c_{\mathrm{R,q}}^4)}{96\,s_{\mathrm{w}}^4\,c_{\mathrm{w}}^4}\,\frac{M_{\mathrm{Z}}^4\,\cos^2\theta}{s^3\sin^2\theta}+\mathcal{O}\left(\frac{1}{s^4}\right), \\
\frac{\mathrm{d}\sigma_{\mathrm{LT}}}{\mathrm{d}\cos\theta} &= \frac{\pi\alpha^2(c_{\mathrm{L,q}}^4+c_{\mathrm{R,q}}^4)}{192\,s_{\mathrm{w}}^4\,c_{\mathrm{w}}^4}\,\frac{16M_{\mathrm{Z}}^2\left(s-4M_{\mathrm{Z}}^2\right)\left(\left(s-2M_{\mathrm{Z}}^2\right)^2+\left(4M_{\mathrm{Z}}^4+4M_{\mathrm{Z}}^2s-2s^2\right)\cos^2\theta+s^2\cos^4\theta\right)}{s\sqrt{1-(4M_{\mathrm{Z}}^2/s)}\left(s\,(4M_{\mathrm{Z}}^2-s)\,\cos^2\theta+(s-2M_{\mathrm{Z}}^2)^2\right)^2} \\
&= \frac{\pi\alpha^2(c_{\mathrm{L,q}}^4+c_{\mathrm{R,q}}^4)}{12\,s_{\mathrm{w}}^4\,c_{\mathrm{w}}^4}\,\frac{M_{\mathrm{Z}}^2}{s^2}+\mathcal{O}\left(\frac{1}{s^3}\right) \\
\frac{\mathrm{d}\sigma_{\mathrm{TT}}}{\mathrm{d}\cos\theta} &= \frac{\pi\alpha^2(c_{\mathrm{L,q}}^4+c_{\mathrm{R,q}}^4)}{192\,s_{\mathrm{w}}^4\,c_{\mathrm{w}}^4}\,\frac{4\left(s-4M_{\mathrm{Z}}^2\right)\left(\left(s-2M_{\mathrm{Z}}^2\right)^2+(36M_{\mathrm{Z}}^4-4M_{\mathrm{Z}}^2s+s^2)\cos^2\theta\right)\sin^2\theta}{\sqrt{1-(4M_{\mathrm{Z}}^2/s)}\left(s\,(4M_{\mathrm{Z}}^2-s)\,\cos^2\theta+(s-2M_{\mathrm{Z}}^2)^2\right)^2} \\
&= \frac{\pi\alpha^2(c_{\mathrm{L,q}}^4+c_{\mathrm{R,q}}^4)}{48\,s_{\mathrm{w}}^4\,c_{\mathrm{w}}^4}\,\frac{1+\cos^2\theta}{s\sin^2\theta}+\mathcal{O}\left(\frac{1}{s^2}\right),
\end{aligned}
\tag{2.22}
$$

where $c_{\mathrm{L,q}}, c_{\mathrm{R,q}}$ are the left- and right-handed couplings of the Z boson to quarks q, and $s_{\mathrm{w}}, c_{\mathrm{w}}$ are the sine and cosine of the EW mixing angle. At a given scattering angle, the expansion in powers of s gives a LL cross-section that is suppressed by $1/s^2$ w.r.t. the TT one and by $1/s$ w.r.t. the mixed one. The suppression of the LL signal can be explained using the Goldstone-boson equivalence theorem [95–98], which relates the amplitudes for longitudinal vector-boson production to those for would-be-Goldstone-boson production at high energies of the vector bosons. Since the couplings of the Goldstone bosons to massless

JHEP10(2021)097

fermions vanish, there are no Feynman diagrams for the production of a pair of neutral would-be Goldstone bosons at LO. Consequently, the amplitude for the production of a pair of longitudinal on-shell Z bosons vanishes in the high-energy limit as $1/s$, and the corresponding cross-section is suppressed w.r.t. the one for purely-transverse and mixed polarization states at large energy [99, 100]. In contrast, the amplitude for longitudinal W^+W^- production is not suppressed in the same way, since the amplitude for the production of a pair of charged Goldstone bosons is finite, thanks to the diagram with an s-channel exchange of a neutral EW boson. These on-shell results indicate a very small purely-longitudinal ZZ signal, which is expected also when including off-shell effects and radiative corrections.

2.4 Numerical tools and input parameters

We study the production of $e^+e^-\mu^+\mu^-$ in LHC proton-proton collisions at a centre-of-mass energy of 13 TeV with NLO QCD and EW accuracy within the SM.

The computation is performed with MoCaNLO, a multi-channel Monte Carlo integrator that has already been used for several multi-boson LHC processes, and in particular for the NLO QCD corrections to polarized W^+W^- and W^+Z production [79, 80]. Tree-level and one-loop SM amplitudes are computed with Recola [101, 102], tensor and scalar loop integrals are reduced and evaluated with Collier [103]. The five-flavour scheme is used for both LO and NLO predictions, and all contributions with external b quarks (both in the initial and the final state) are included in the computation. All quarks and leptons are assumed to be massless, and no quark mixing is understood (unit CKM matrix). The pole masses M_V of weak bosons are computed from the corresponding on-shell masses M_V^{OS} [104],

$$\begin{aligned} M_{\mathrm{W}}^{\mathrm{OS}} &= 80.379\,\mathrm{GeV}, & \Gamma_{\mathrm{W}}^{\mathrm{OS}} &= 2.085\,\mathrm{GeV}, \\ M_{\mathrm{Z}}^{\mathrm{OS}} &= 91.1876\,\mathrm{GeV}, & \Gamma_{\mathrm{Z}}^{\mathrm{OS}} &= 2.4952\,\mathrm{GeV}, \end{aligned} \tag{2.23}$$

via the well-known expressions [82],

$$M_V = \frac{M_V^{\mathrm{OS}}}{\sqrt{1+(\Gamma_V^{\mathrm{OS}}/M_V^{\mathrm{OS}})^2}}\,, \qquad \Gamma_V = \frac{\Gamma_V^{\mathrm{OS}}}{\sqrt{1+(\Gamma_V^{\mathrm{OS}}/M_V^{\mathrm{OS}})^2}}. \tag{2.24}$$

The EW coupling α is fixed in the G_μ scheme [86],

$$\alpha = \frac{\sqrt{2}}{\pi}\,G_\mu M_{\mathrm{W}}^2\left(1-\frac{M_{\mathrm{W}}^2}{M_{\mathrm{Z}}^2}\right), \qquad G_\mu = 1.16638\cdot 10^{-5}\,\mathrm{GeV}^{-2}. \tag{2.25}$$

The top-quark and Higgs-boson masses are set to

$$M_{\mathrm{H}} = 125\,\mathrm{GeV}, \qquad m_{\mathrm{t}} = 173\,\mathrm{GeV}\,. \tag{2.26}$$

The complex-mass scheme is utilized for the treatment of unstable particles [85–87, 105]. The subtraction of infrared singularities is achieved in the dipole formalism [91–93] both for QCD and EW corrections. The values of parton distribution functions (PDFs) and

JHEP10(2021)097

the running of α_s are passed to MoCaNLO via the LHAPDF6 interface [106]. We choose the NNPDF31_nlo_as_0118_luxQED PDF set [107, 108], which understands $\alpha_s(M_Z) = 0.118$ and includes also the modelling of the photon luminosity in the proton [108]. The same PDF set is used for both LO- and NLO-accurate results. Initial-state collinear singularities are absorbed in PDFs via the $\overline{\text{MS}}$ scheme. The factorization and renormalization scales are simultaneously set to the Z-boson pole mass, i.e. $\mu_R = \mu_F = M_Z$.

2.5 Kinematic selections

Photon- and jet-clustering is performed with the anti-k_T algorithm [109]. Recombination is done for particles with a maximum rapidity of 5. In particular, photons are recombined with charged leptons $\ell = e, \mu$ if

$$\Delta R_{\gamma\ell} = \sqrt{\Delta y_{\gamma\ell}^2 + \Delta\phi_{\gamma\ell}^2} < 0.1. \tag{2.27}$$

QCD jets can only arise from real initial-state radiation and cannot generate singular configurations with the final-state leptons. Their kinematics is not constrained by any angular-distance cut.

Following a similar approach as in ref. [79], we have considered two sets of cuts, a first one (label INC) that is rather inclusive in the kinematics of final-state leptons and a second one (label FID) that mimics the fiducial region used in the latest ATLAS measurement [10]. The INC setup just involves

- a technical cut on the transverse momentum of each charged lepton, $p_{T,\ell} > 0.001\,\text{GeV}$;
- an invariant-mass cut on the two pairs of opposite-sign, same-flavour leptons, $|M_{\ell^+\ell^-} - M_Z| < 10\,\text{GeV}$.

The second cut is essential to enhance the on-shell production of two Z bosons, i.e. to reduce the photon contamination and other non-doubly-resonant contributions.

The FID setup involves

- a minimum transverse-momentum and a maximum-rapidity cut for the electron and the positron, $p_{T,e^\pm} > 7\,\text{GeV}$, $|\eta_{e^\pm}| < 2.47$;
- a minimum transverse-momentum and a maximum-rapidity cut for the muon and the antimuon, $p_{T,\mu^\pm} > 5\,\text{GeV}$, $|\eta_{\mu^\pm}| < 2.7$;
- a minimum transverse-momentum cut on the leading, $p_{T,\ell_1} > 20\,\text{GeV}$, and on the subleading charged lepton, $p_{T,\ell_2} > 10\,\text{GeV}$ (sorted according to transverse momentum);
- a rapidity-azimuthal-angle separation between any two leptons, $\Delta R_{\ell\ell'} > 0.05$;
- an invariant-mass cut on the two pairs of opposite-sign, same-flavour leptons, $|M_{\ell^+\ell^-} - M_Z| < 10\,\text{GeV}$;
- a minimum invariant-mass cut on the four-lepton system, $M_{4\ell} > 180\,\text{GeV}$.

JHEP10(2021)097

We have checked numerically that the effect of the $M_{4\ell} > 180\,\text{GeV}$ cut is to enhance the on-shell ZZ production even in the absence of the $|M_{\ell^+\ell^-} - M_\text{Z}| < 10\,\text{GeV}$ cut: under these conditions the non-doubly-resonant background would account for 15% of the full result. The joint effect of $M_{4\ell} > 180\,\text{GeV}$ and $|M_{\ell^+\ell^-} - M_\text{Z}| < 10\,\text{GeV}$ cuts reduces the non-doubly-resonant background to less than 1% of the full cross-section.

3 Results

We now present the numerical results of our computation. In section 3.1 we consider the INC setup and NLO EW accuracy. These results provide both a validation of the calculation and a first assessment of how the polarization structure of ZZ production is modified by EW corrections. The complete NLO results, combined with loop-induced contributions, and a discussion of the relative impact of NLO EW and QCD corrections are then shown for the FID setup in section 3.2.

3.1 Inclusive phase-space: NLO EW results

The results presented in this section have been obtained in the INC setup described in section 2.5.

Before tackling the polarized signals, we discuss the differences between the full calculation and the DPA-approximated one for unpolarized production. The proper functioning of the subtraction of EW IR singularities in the DPA calculation has been tested by varying the subtraction parameter α_dip [110] between 10^{-2} and 1. The sum of real-subtracted and integrated-dipole contributions has been found to be independent of α_dip, demonstrating that the combined application of DPA techniques presented in section 2.1 and section 2.2 works in the desired manner. In table 1 we show the various contributions to the NLO EW cross-section, separating them into contributions of partonic channels. The LO DPA result is roughly 1.2% smaller than the full one, in agreement with the expected difference of order $\Gamma_\text{Z}/M_\text{Z} = 2.7\%$ (intrinsic accuracy of the DPA). Note that when performing the DPA for Z bosons, an on-shell constraint ($|M_{\ell^+\ell^-} - M_\text{Z}| < 10\,\text{GeV}$ in our case) is crucial to suppress the photon contamination to the leptonic decays, which is included in the full but not in the DPA result [72]. At LO the full result receives a very small contribution from the $\gamma\gamma$-induced partonic process.

The EW corrections in the $q\bar{q}$ partonic channel dominate the total NLO EW correction, and the DPA underestimates (in size) the full result by 2.2%. This difference comes mostly from the large virtual and integrated-dipole contributions ($-2.610\,\text{fb}$ in the full calculation) and is enhanced by the relative sign between virtual and real corrections. Note that the real contributions are small and positive (0.337 fb in the full calculation) and are approximated by the DPA within 0.9%.

The γq and $\gamma\bar{q}$ partonic channels participate in the calculations as real corrections that involve only initial-state singularities. A marked difference is found between the DPA numerical result and the full one for such partonic channels, since the real-subtracted contributions in the full case embed additional dipoles compared to those that are included in the DPA, corresponding to the non-doubly-resonant contributions with underlying $\gamma\gamma$ as Born

JHEP10(2021)097

	full [fb]	ratio	DPA [fb]	ratio	(DPA/full − 1)
$\sigma_{\text{LO}}^{q\bar{q}}$	20.993(1)	100%	20.749(1)	100%	−1.16%
$\sigma_{\text{LO}}^{\gamma\gamma}$	0.01509(1)	0.07%	0	0%	–
σ_{LO}	21.008(1)	100.07%	20.749(1)	100%	−1.23%
$\Delta\sigma_{\text{EW}}^{q\bar{q}}$	−2.273(1)	−10.83%	−2.2235(6)	−10.72%	−2.18%
$\Delta\sigma_{\text{EW}}^{\gamma q,\gamma\bar{q}}$	−0.00579(8)	−0.03%	0.000850(1)	0.004%	–
$\Delta\sigma_{\text{EW}}^{\gamma\gamma}$	0.00115(2)	0.005%	0	0%	–
$\Delta\sigma_{\text{EW}}$	−2.277(1)	−10.85%	−2.2226(6)	−10.71%	−2.38%
$\sigma_{\text{NLO}_{\text{EW}}}$	18.731(2)	89.22%	18.526(1)	89.29%	−1.09%

Table 1. Contributions to the NLO EW cross-section for four-lepton production at the LHC in the full and DPA (unpolarized) computation. Ratios are computed relatively to the LO result for the $q\bar{q}$ partonic channel. The INC setup is understood (see section 2.5). Numerical errors are shown in parentheses.

partonic channel [see figure 5(b)]. This causes the presence of additional integrated dipoles from the $\gamma\gamma$ Born contribution that are absent in the DPA calculation. Note that the EW corrections to the $\gamma\gamma$-induced process account for less than 0.01% of the LO cross-section. Summing all contributions, the NLO EW cross-section in the DPA is 1.1% smaller than the full one, indicating a small non-doubly-resonant background from photon contamination and missing off-shell effects, in particular in the region between $162\,\text{GeV} < M_{4\ell} < 182\,\text{GeV}$ where the DPA contribution vanishes. The overall EW corrections account for −10.8% (−10.7%) of the full (DPA) LO cross-section. This large effect is mostly due to the on-shell constraint imposed on the final-state leptons. Similar EW corrections have been obtained with analogous invariant-mass constraints in ref. [36]. If a looser invariant-mass cut is applied, the impact of EW corrections is smaller [18, 19].

The difference between the full and the unpolarized DPA calculations implies that the non-doubly-resonant background is very small ($\approx 1\%$), and on-shell ZZ production dominates the four-lepton production in the considered setup. Larger effects may arise in differential distributions, as observed in W^+W^- and WZ production [79, 80] where at large transverse momentum single-resonant contributions become sizeable, generating large non-doubly-resonant backgrounds. However, in the four-charged-lepton channel the single-resonant contributions are much more suppressed than in the presence of final-state neutrinos, thanks to the possibility of constraining both Z bosons to be almost on-shell via physical invariant-mass cuts.

We now consider the ZZ signals where both bosons have definite polarization states (L or T). In table 2 we show the LO and NLO EW integrated cross-sections for the unpolarized and polarized process. Polarizations are defined either in the CM or in the LAB frame. The interference among polarization states is evaluated as the difference between the unpolarized DPA result (which, by definition, contains also interference terms) and the

JHEP10(2021)097

mode	σ_{LO} [fb]	f_{LO}	$\sigma_{\text{NLO}_{\text{EW}}}$ [fb]	$f_{\text{NLO}_{\text{EW}}}$	δ_{EW}
full	21.008(1)	–	18.731(2)	–	−10.8%
unpol.	20.749(1)	100%	18.526(1)	100%	−10.7%
polarizations defined in the CM frame					
$Z_L Z_L$	1.2049(3)	5.81%	1.0820(2)	5.84%	−10.2%
$Z_L Z_T$	2.3886(2)	11.51%	2.1486(3)	11.60%	−10.0%
$Z_T Z_L$	2.3887(2)	11.51%	2.1488(3)	11.60%	−10.0%
$Z_T Z_T$	14.737(1)	71.03%	13.117(1)	70.80%	−11.0%
interf.	0.030(2)	0.14%	0.029(2)	0.16%	–
polarizations defined in the LAB frame					
$Z_L Z_L$	0.32525(6)	1.57%	0.29156(7)	1.58%	−10.4%
$Z_L Z_T$	5.9542(5)	28.70%	5.3507(6)	28.88%	−10.1%
$Z_T Z_L$	5.9541(4)	28.70%	5.3505(6)	28.88%	−10.1%
$Z_T Z_T$	8.4752(5)	40.85%	7.4956(6)	40.46%	−11.6%
interf.	0.040(2)	0.19%	0.038(2)	0.20%	–

Table 2. Integrated cross-sections in the INC setup (see section 2.5) for unpolarized and doubly-polarized ZZ production at the LHC at LO and NLO EW accuracy. The polarization fractions f_{LO}, $f_{\text{NLO}_{\text{EW}}}$ are computed as ratios of polarized cross-sections over the unpolarized DPA one at LO and at NLO EW, respectively. The NLO EW corrections are shown in the right-most column, as percentages relative to LO cross-sections (δ_{EW}). The full results are obtained including all doubly-resonant and non-doubly-resonant contributions, while all other results are based on the DPA described in section 2.2. Interference contributions are obtained by subtracting the sum of polarized results from the DPA unpolarized one. Numerical errors are shown in parentheses.

sum over doubly-polarized results. For integrated cross-sections, interferences are found to be at the 0.2% level both at LO and at NLO EW.

It has been shown [80] that the spin correlations between the two bosons can be sizeable in the CM-frame definition of polarization and enhanced if both bosons are in a definite polarization state. Therefore, the sum over doubly-polarized modes is expected to differ from the unpolarized DPA result more than the sum over singly-polarized modes, i.e. larger interference effects are present.

Up to the correlation effects mentioned above, vanishing interferences are expected for the inclusive case at LO, where the two-body decay of each Z boson enables an exact analytic expression of the unpolarized DPA cross-section in terms of a sum over polarized

JHEP10(2021)097

contributions [66, 67]:

$$\frac{1}{\sigma}\frac{\mathrm{d}\sigma}{\mathrm{d}\cos\theta^*_{\ell^+}} = \frac{3}{4}f_\mathrm{L}\left(1-\cos^2\theta^*_{\ell^+}\right) + \frac{3}{8}f_-\left(1+\cos^2\theta^*_{\ell^+} - 2\cos\theta^*_{\ell^+}\frac{c^2_{\mathrm{L},\ell}-c^2_{\mathrm{R},\ell}}{c^2_{\mathrm{L},\ell}+c^2_{\mathrm{R},\ell}}\right) + \frac{3}{8}f_+\left(1+\cos^2\theta^*_{\ell^+} + 2\cos\theta^*_{\ell^+}\frac{c^2_{\mathrm{L},\ell}-c^2_{\mathrm{R},\ell}}{c^2_{\mathrm{L},\ell}+c^2_{\mathrm{R},\ell}}\right), \tag{3.1}$$

where $\theta^*_{\ell^+}$ is the decay angle of the antilepton in the rest frame of the corresponding Z boson (with momentum equal to the sum of the two lepton momenta) computed w.r.t. the Z direction in the CM (LAB) frame for polarization vectors defined in the CM (LAB) frame. The coefficients f_L, f_+, f_- are polarization fractions, and $c_{\mathrm{L},\ell}$, $c_{\mathrm{R},\ell}$ are the left- and right-handed couplings of the Z boson to leptons. This expression can be derived assuming that the complete phase-space of decay products is available, such that interference terms vanish upon integration over the azimuthal decay angle [71]. Projecting the $\cos\theta^*_{\ell^+}$ distribution onto suitable polynomials in $\cos\theta^*_{\ell^+}$ [66, 67, 71], it is possible to extract the polarization fractions for the Z boson and compare the result with the one obtained by directly simulating polarized Z bosons with the Monte Carlo. In the INC setup, this comparison yields a very good agreement for the LO predictions as well as for other n-body contributions (virtual, integrated dipoles) to the NLO EW cross-section. While doubly-polarized polarization fractions cannot be obtained from projections on parametrizations of unpolarized cross-sections like eq. (3.1), their definition is straightforward based on eq. (2.21). The LO interference estimated from the sum of the thus defined doubly-polarized Monte Carlo predictions is not identically zero (as it would be summing singly-polarized signals) due to the above-mentioned correlation effects.

In the presence of final-state real corrections, eq. (3.1) does not hold anymore, as one Z boson decays into three particles, therefore projecting the $\cos\theta^*_{\ell^+}$ distributions in the same way as at LO gives results that have nothing to do with polarization fractions [69]. Furthermore, in the presence of photons radiated off decay leptons, the interferences among polarization states are not vanishing anymore, even if the complete phase-space is available for the three-body decay. For example, if we consider a polarized Z boson that decays into $\mathrm{e}^+\mathrm{e}^-\gamma$, the polarization fractions from Monte Carlo simulations (f_i^MC) and those obtained projecting on $\cos\theta^*_{\mathrm{e}^+}$ distributions (f_i^proj) read

$$\begin{aligned} f_\mathrm{L}^\mathrm{MC} &= 0.1437(3), & f_\mathrm{T}^\mathrm{MC} &= 0.837(1) \\ f_\mathrm{L}^\mathrm{proj} &= 0.317(1), & f_\mathrm{T}^\mathrm{proj} &= f_+^\mathrm{proj} + f_-^\mathrm{proj} = 0.683(4)\,. \end{aligned} \tag{3.2}$$

The discrepancy between the two evaluations of polarization fractions is large, indicating that real contributions to polarized signals can only be computed with polarized amplitudes in the Monte Carlo, even in a very inclusive setup like the one that is understood here. Note that the sum of polarization fractions extracted with $\cos\theta^*_{\mathrm{e}^+}$ projections gives 1 by definition, while the sum of polarization fractions (ratios of polarized cross-sections over the DPA unpolarized one) computed with the Monte Carlo suggests that a 2% effect comes

JHEP10(2021)097

from interferences. However, although interferences in FSR1/2 corrections are at the 2% level, when summing all EW corrections to ZZ production this effect is hardly visible in the NLO EW total cross-section, since the real corrections are small compared to the virtual ones. This explains why even at NLO EW the overall interferences are small (0.16% and 0.20% for polarizations defined in the CM and the LAB frame, respectively).

It is worth noting that in both polarization definitions the relative NLO EW corrections stay between -10% and -12% for all modes, with slighly more sizeable corrections for the LL and TT modes than for the mixed ones. In both definitions, the polarization fractions are hardly modified by NLO EW effects: the modes with at least one longitudinal boson are slightly enhanced, while the TT mode is mildly diminished. In the CM-frame definition, the LL and the mixed modes are of the same order of magnitude (5.8% and 11.6% respectively), while the TT mode is dominant. This situation is completely changed in the LAB definition, as the LL mode accounts for just 1.6%, while the sum of mixed contributions gives 57.8% of the total. This difference, in a similar fashion as in W^+Z production [80], is due to the fact that part of the LL contributions defined in the CM frame (where the polarization vectors just depend on one Z-boson momentum, thanks to the back-to-back kinematics) become transverse when boosting to the LAB frame, giving a more involved dependence on kinematic quantities. This has also the effect of reducing the TT component in favour of the mixed ones.

The polarized results for differential cross-sections can embed effects that are rather different from those obtained at the integrated level, in particular concerning the interference effects. In figures 6–7, we study the distributions in a number of LHC observables, focusing on the shapes and normalizations of differential cross-sections in top panels, the impact of EW corrections in middle panels, and the impact of non-doubly-resonant (grey curves) and interference effects (grey vs. magenta curves) in bottom panels.

In figure 6 we consider the decay angle of the positron in the Z rest frame, which has been introduced in eq. (3.1). This angular variable is expected to be highly sensitive to the polarization of the first Z boson. At NLO EW the Z boson is understood as the system of the two dressed leptons (e^+e^-), i.e. after photon recombination, in order to ensure the IR safety of the variable. The angle $\theta^*_{e^+}$ can be computed w.r.t. the Z-boson direction in the CM frame or w.r.t. the Z-boson direction in the LAB frame. For both definitions of $\theta^*_{e^+}$, the non-doubly-resonant background effects are flat and equal to those found at the integrated level. If $\theta^*_{e^+}$ is computed w.r.t. the Z-boson direction in the same frame where polarization vectors are defined, the analytic expression for the differential distribution is known at LO [see eq. (3.1)] and interferences are expected to vanish. This is the case in figures 6(a) and 6(d), where also at NLO EW the interferences are at the few-permille level owing to small FSR1/2 real contributions. Both in figure 6(a) and in figure 6(d), the LL and LT distributions display the same shape, which has a $\sin^2\theta^*_{e^+}$ functional dependence on the angle. In figure 6(a), the TL and TT distributions exhibit the same symmetric shape, because of left-right symmetry of Z-boson production in the CM frame.[1] On the

[1]Owing to Bose symmetry and the explicit form of the polarization vectors, left- and right-handed Z bosons are produced with equal probabilities in the CM frame.

JHEP10(2021)097

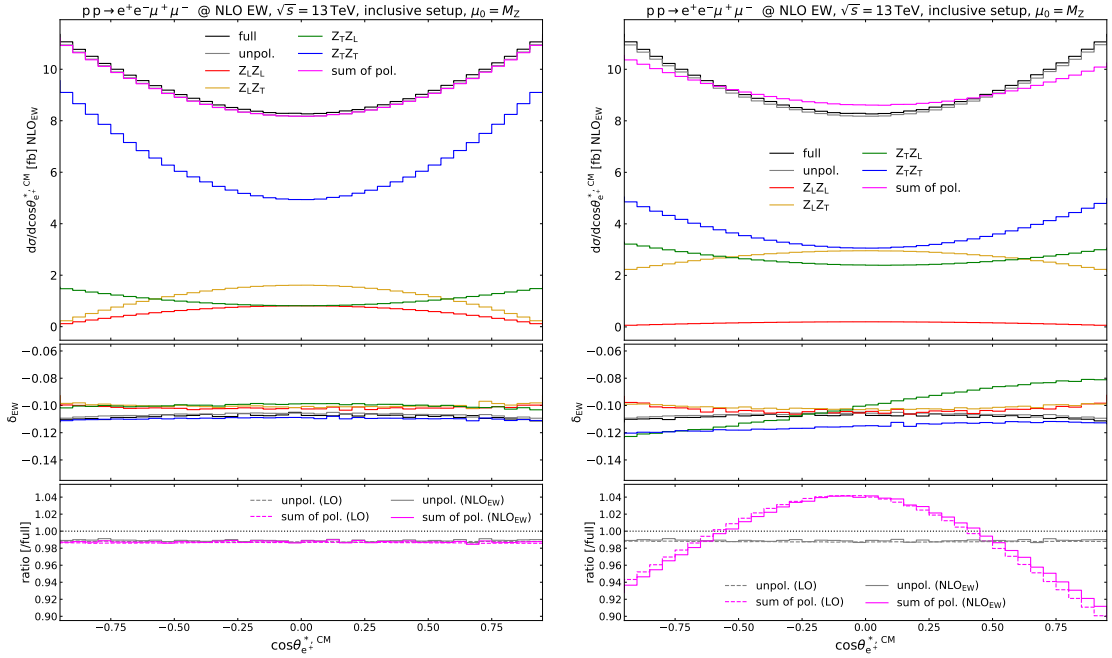

(a) $\cos\theta^{*,\mathrm{CM}}_{e^+}$, CM

(b) $\cos\theta^{*,\mathrm{CM}}_{e^+}$, LAB

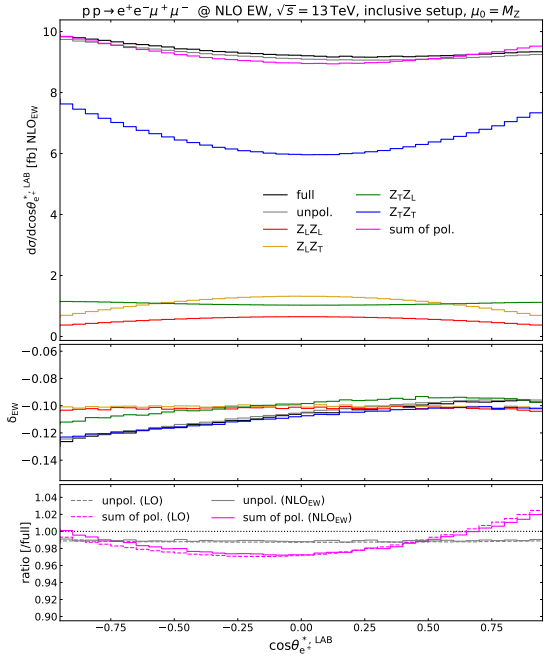

(c) $\cos\theta^{*,\mathrm{LAB}}_{e^+}$, CM

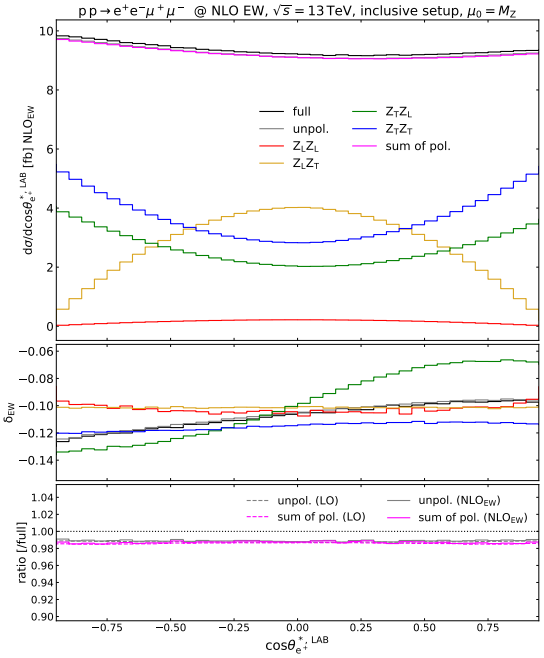

(d) $\cos\theta^{*,\mathrm{LAB}}_{e^+}$, LAB

Figure 6. Distributions in the cosine of the polar decay angle θ^* of the positron in its corresponding Z-boson rest frame computed w.r.t. the Z-boson spatial direction in the CM frame (a,b) and in the LAB frame (c,d). Polarizations are defined in the CM (a,c) and in the LAB (b,d) frame. Unpolarized and doubly-polarized results are shown for ZZ production at the LHC in the inclusive setup described in section 2.5. From top down: $\mathrm{NLO_{EW}}$ differential cross-sections, EW corrections relative to LO (δ_{EW}), and ratios of DPA over the full result.

JHEP10(2021)097

contrary, in figure 6(d) the TL distribution is not symmetric, due to a different left- and right-polarization content for the first boson in the presence of a recoiling longitudinal boson. The difference in shape between the TL and the TT curves indicates that the polarization of the first boson is affected differently by different polarization states of the second boson.

If both the polarization vectors and the $\theta^*_{e^+}$ angle are defined in the CM frame [figure 6(a)], the relative EW corrections are flat for both polarized and unpolarized signals. On the contrary, for the LAB-frame definition [figure 6(d)], the EW corrections enhance the various polarized signals differently. They are rather uniform for the LL, LT and TT components, while for the TL component they increase by about 6% going from the anti-collinear configuration towards the collinear one. Therefore, differences between the two polarization definitions are found at the level of EW corrections, even for very inclusive variables like decay angles. Thanks to the flat behaviour of EW corrections, the CM-frame definition seems preferable over the LAB-frame one.

If polarizations are defined in the CM (LAB) frame, the distributions in the angle $\theta^*_{e^+}$ computed w.r.t. the Z direction in the LAB (CM) frame receive large interference effects, as can be appreciated in figures 6(b)–6(c). The interference pattern is different in the two cases: interferences are in fact negative in the (anti)collinear configuration in figure 6(c) but positive in figure 6(b). A difference in size is also evident: if polarizations are defined in the CM frame and the decay angle is defined w.r.t. the Z direction in the LAB frame [figure 6(c)], the interferences give at most a 3% effect, while in the opposite case they give up to 6% effects.

The distribution in the decay angle θ^*_ℓ is highly sensitive to the polarization state of the corresponding Z boson. However, in order to avoid noticeable interference effects, it is essential that the definition of the angle is consistent with the frame where polarizations are defined, as in the case of figures 6(a) and 6(d).

In figure 7 we consider the azimuthal distance between the positron and the muon computed w.r.t. to the beam axis. The two particles are decay products of different bosons, and tend to be produced with $\Delta\phi_{e^+\mu^-} = \pi$. For both the unpolarized and the polarized distributions the EW corrections monotonically decrease with increasing $\Delta\phi_{e^+\mu^-}$. For unpolarized cross-sections, EW corrections range between -9% and -13%. For polarizations defined in the CM frame, all polarized cross-sections receive the same flat corrections for $\Delta\phi_{e^+\mu^-} < \pi/2$. For $\Delta\phi_{e^+\mu^-} > \pi/2$, the EW corrections for TT decrease along with the unpolarized one, while those for other polarizations remain rather flat. A similar behaviour is found in the LAB frame, where all polarized curves (except from the TT one) are pretty flat in the whole angular range.

The two definitions of polarizations lead to very different interference patterns to this angular variable. In the CM-frame definition, the interferences never exceed 0.8%, with mild differences between the LO and the NLO EW results. In the LAB definition, the NLO EW interferences are positive for $\Delta\phi_{e^+\mu^-} < \pi/2$ and amount to 2.5% at $\Delta\phi_{e^+\mu^-} = 0$, they are negative but less sizeable in the rest of the spectrum.

In figure 8 we consider differential cross-sections in the positron transverse momentum. The purely-longitudinal signal is strongly suppressed at large transverse momentum

JHEP10(2021)097

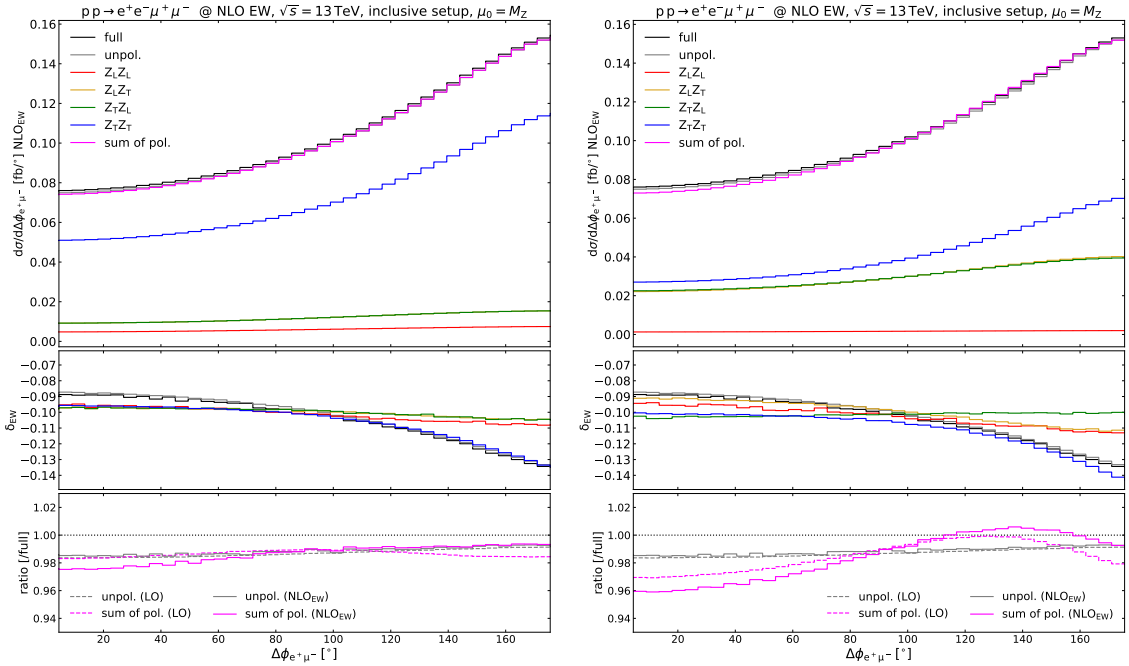

(a) $\Delta\phi_{e^+\mu^-}$, CM (b) $\Delta\phi_{e^+\mu^-}$, LAB

Figure 7. Distributions in the azimuthal separation between the positron and the muon. Polarizations are defined the CM (a) and in the LAB (b) frame. Same structure as in figure 6.

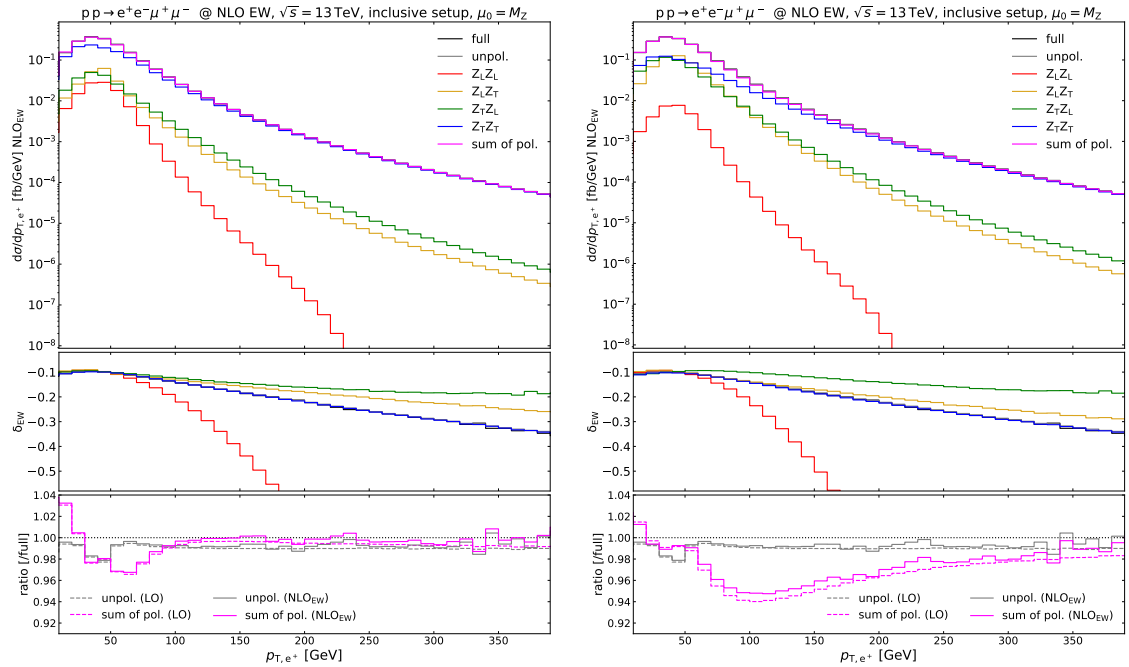

(a) p_{T,e^+}, CM (b) p_{T,e^+}, LAB

Figure 8. Distributions in the positron transverse momentum. Polarizations are defined the CM (a) and in the LAB (b) frame. Same structure as in figure 6.

JHEP10(2021)097

already at LO [100] and is also characterized by huge and negatively-increasing EW corrections for both polarization definitions. Around 280 GeV the negative virtual corrections exceed the sum of Born and real contributions, implying that the truncation of the perturbative series at order $\mathcal{O}(\alpha^5)$ is not sufficient at large transverse momentum. We have checked numerically that the same effect can be reproduced simulating the production of longitudinal on-shell bosons (no decays), which was also addressed in ref. [17]. The longitudinal signal is suppressed by $1/s$ and $1/s^2$ w.r.t. the mixed and the TT contributions, respectively, both at LO and in NLO real corrections, which manifests itself by vanishing amplitudes for neutral Goldstone-boson pair production at tree level. On the contrary, some one-loop diagrams give non-vanishing contributions to Goldstone-boson amplitudes, which at NLO are interfered with tree-level amplitudes. Including the squares of such weak one-loop contributions [formally at order $\mathcal{O}(\alpha^6)$] makes the cross-section positive even at large transverse momentum [17]. However, the smallness of polarized signals at large $p_{\mathrm{T,Z}}$ renders this region definitely out of reach even with increased LHC luminosity. Similar effects can be found in the distributions in the lepton-pair transverse momentum, as well as in the four-lepton invariant mass.

The TT polarization state dominates already at moderate transverse momentum: in the CM-frame definition, the mixed states are one order of magnitude smaller than the TT one already at $p_{\mathrm{T,e^+}} \approx 100\,\mathrm{GeV}$, despite less sizeable EW corrections. In the LAB-frame definition, the mixed states and the TT one have similar size in the soft region of the spectrum. It is interesting to observe the differences in the interference pattern between the two polarization definitions. In the CM-frame definition they amount to $\pm 3\%$ in the soft region, while they are almost negligible in the tail. In the LAB-frame definition, interferences are positive and more sizeable (at most 6%) even at moderate-p_{T}.

Although the interference effects account for 0.2% of the integrated cross-section, they can give more sizeable effects at the differential level, even in the case of inclusive variables. This holds in particular when polarizations are defined in the LAB frame. The impact of the non-doubly-resonant background on the considered distributions is not so different from the one found for the total cross-section. The NLO EW corrections significantly distort the distribution shapes for both polarized and unpolarized signals, with moderate effects in angular variables and dramatic effects in the tails of transverse-momentum and invariant-mass variables.

3.2 Fiducial phase-space: complete NLO results

Thanks to the back-to-back kinematics at LO, the definition of polarizations in the CM frame represents a natural choice for di-boson production. It gives an enhanced LL contribution, rather small mixed contributions, and less sizeable interference effects than the polarization definition in the LAB frame. Therefore, we only present results for the CM-frame definition in the fiducial setup.

The realistic cuts applied in the FID setup are rather loose in the lepton transverse momentum and R distance. The decrease of the inclusive cross-section due to the fiducial cuts is mostly due to the rapidity cuts, which also introduce an asymmetry between the two Z bosons ($|y_{\mathrm{e}^\pm}| < 2.47$ and $|y_{\mu^\pm}| < 2.7$). Once the invariant-mass cut on the four-

JHEP10(2021)097

mode	$\sigma_{\rm LO}$ [fb]	$\delta_{\rm QCD}$	$\delta_{\rm EW}$	$\delta_{\rm gg}$	$\sigma_{\rm NLO_+}$ [fb]	$\sigma_{\rm NLO_\times}$ [fb]
full	$11.1143(5)^{+5.6\%}_{-6.8\%}$	+34.9%	−11.0%	+15.6%	$15.505(6)^{+5.7\%}_{-4.4\%}$	$15.076(5)^{+5.5\%}_{-4.2\%}$
unpol.	$11.0214(5)^{+5.6\%}_{-6.8\%}$	+35.0%	−10.9%	+15.7%	$15.416(5)^{+5.7\%}_{-4.4\%}$	$14.997(4)^{+5.5\%}_{-4.2\%}$
$\rm Z_L Z_L$	$0.64302(5)^{+6.8\%}_{-8.1\%}$	+35.7%	−10.2%	+14.5%	$0.9002(6)^{+5.5\%}_{-4.3\%}$	$0.8769(5)^{+5.4\%}_{-4.1\%}$
$\rm Z_L Z_T$	$1.30468(9)^{+6.5\%}_{-7.7\%}$	+45.3%	−9.9%	+2.8%	$1.8016(9)^{+4.3\%}_{-3.5\%}$	$1.7426(8)^{+4.1\%}_{-3.3\%}$
$\rm Z_T Z_L$	$1.30854(9)^{+6.5\%}_{-7.7\%}$	+44.3%	−9.9%	+2.8%	$1.7933(9)^{+4.3\%}_{-3.4\%}$	$1.7355(8)^{+4.0\%}_{-3.2\%}$
$\rm Z_T Z_T$	$7.6425(3)^{+5.2\%}_{-6.4\%}$	+31.2%	−11.2%	+20.5%	$10.739(4)^{+6.2\%}_{-4.7\%}$	$10.471(3)^{+6.1\%}_{-4.6\%}$

Table 3. Integrated cross-sections in the fiducial setup (see section 2.5) for unpolarized and doubly-polarized ZZ production at the LHC at LO and NLO accuracy. Polarizations are defined in the CM frame. Corrections are shown as percentages relative to LO cross-sections. The NLO cross-sections include NLO EW and QCD corrections and the loop-induced gg contribution, combined with the additive (+) or multiplicative (×) prescription. Theory uncertainties from 7-point scale variations are shown as percentages for the LO and NLO results. Parentheses contain integration errors.

lepton system, $M_{4\ell} > 180\,\text{GeV}$, is applied, the cuts on the leading and sub-leading lepton do not modify much the event rate. The presence of lepton cuts is expected to give larger interference effects than in the inclusive case [67, 68, 71].

In table 3 we show the integrated cross-sections in the FID setup, both for polarized and unpolarized signals. We have included NLO effects of EW and QCD type, as well as the loop-induced contribution from the gg partonic channel. Starting from the LO results, we have combined the higher-order corrections both with an additive and with a multiplicative approach [31]:

$$\mathrm{d}\sigma_{\rm NLO_+} = \mathrm{d}\sigma_{\rm LO}\,(1 + \delta_{\rm QCD} + \delta_{\rm EW}) + \mathrm{d}\sigma_{\rm LO}\delta_{\rm gg}\,, \tag{3.3}$$

$$\mathrm{d}\sigma_{\rm NLO_\times} = \mathrm{d}\sigma_{\rm LO}\,(1 + \delta_{\rm QCD})\,(1 + \delta_{\rm EW}) + \mathrm{d}\sigma_{\rm LO}\delta_{\rm gg}\,, \tag{3.4}$$

where we have defined the relative corrections in the following way:

$$\delta_{\rm EW} = \frac{\mathrm{d}\Delta\sigma_{\rm EW}}{\mathrm{d}\sigma_{\rm LO}}\,, \qquad \delta_{\rm QCD} = \frac{\mathrm{d}\Delta\sigma_{\rm QCD}}{\mathrm{d}\sigma_{\rm LO}}\,, \qquad \delta_{\rm gg} = \frac{\mathrm{d}\sigma_{\rm gg}}{\mathrm{d}\sigma_{\rm LO}}\,. \tag{3.5}$$

The cross-section $\sigma_{\rm LO}$ includes LO contributions in the $q\bar{q}$ and $\gamma\gamma$ partonic channels. The quantity $\Delta\sigma_{\rm EW}$ embeds all EW corrections in the $q\bar{q}$, $\gamma\gamma$, γq and $\gamma\bar{q}$ channels, while $\Delta\sigma_{\rm QCD}$ furnishes the QCD corrections in the $q\bar{q}$, $\mathrm{g}q$ and $\mathrm{g}\bar{q}$ channels. Loop-induced contributions from the gg partonic channel are included in $\sigma_{\rm gg}$. The combination of corrections according to eqs. (3.3) and (3.4) is performed on a bin-by-bin basis. The difference between the multiplicative and the additive results ($= \delta_{\rm EW}\,\delta_{\rm QCD}\,\mathrm{d}\sigma_{\rm LO}$) gives an approximated estimate of the mixed EW-QCD corrections of order $\mathcal{O}(\alpha^5\alpha_{\rm s})$. The multiplicative approach is generally preferable at large partonic energies ($\hat{s} \gg M_{\rm Z}^2$) as the dominant EW corrections factorize w.r.t. the QCD effects. In principle, for the factorization properties of EW and QCD corrections, the multiplicative approach should be applied to the $q\bar{q}$ contributions

JHEP10(2021)097

only. However, we have checked numerically that, due the smallness of photon-induced contributions, this further refinement of the multiplicative prescription agrees at the per-mille level with results obtained applying eq. (3.4), both for integrated cross-sections and for differential distributions. This conclusion was also found when combining NNLO QCD and NLO EW corrections to ZZ production [31]. Therefore, in the following we stick to the simple multiplicative prescription of eq. (3.4).

As in the inclusive setup (see table 2), the EW corrections are negative and sizeable, accounting for about -10% of the LO results for all polarized signals with at least one longitudinal boson, about -11% for the purely-transverse and unpolarized signals. The QCD corrections give the largest correction to LO cross-sections, ranging between $+30\%$ and $+45\%$ for the various polarized and unpolarized signals. Such corrections are particularly large for the mixed states, an effect that characterizes also W^+Z production [80]. The loop-induced contribution from the gluon-gluon partonic channel gives a sizeable enhancement to the LL and TT signals of 15% and 20%, respectively. For mixed polarization modes, this gluon-initiated contribution is only at the level of 3%.

The additive combination of NLO corrections and loop-induced contributions results in an enhancement of the LO cross-section of about 40% for all signals, while the multiplicative combination gives a smaller overall correction of about 35% for all signals. At the level of total cross-sections the difference between the additive and multiplicative results is about 2.8%, which is smaller than NLO scale uncertainties.

The uncertainties of the fiducial NLO cross-section from 7-point scale variations are strongly affected by the gluon-induced partonic channel. In fact, the noticeable reduction of scale uncertainties from LO to NLO QCD (from order 5% to order 2%) is counterbalanced by 25% scale uncertainties of the gluon-induced contribution, resulting in only a mild reduction of the combined scale uncertainties. The most noticeable scale-uncertainty reduction is found for the mixed polarization states (from 7% at LO to 4% at NLO), owing to the small size of loop-induced contributions.

Thanks to the joint effect of the four-lepton and lepton-pair invariant mass cuts, the non-doubly-resonant background accounts for just 0.8% of the full result at LO and even less when including radiative corrections (0.5% for $\text{NLO}_\times$). The interferences are larger than in the inclusive setup. The polarization fractions and the impact of the interferences are shown in table 4, as relative percentages of the DPA unpolarized result. Interference effects are at the level of 1% both at LO and at NLO, but larger effects could be present in differential results. They are particularly small for the gluon-induced process. The LO polarization fractions are roughly conserved when including NLO EW corrections, with the LL contribution accounting for 6% of the total, which is dominated by purely-transverse states (70%). The NLO QCD fractions show a 0.8% increase in the mixed cases, and correspondingly a 3% decrease in the TT one. The polarization fractions for the loop-induced contribution differ greatly from those found in $q\bar{q}$ channels, with very small mixed contributions of about 2% each and a longitudinal fraction of about 5%, which mostly comes from box diagrams involving top loops, and a 90% TT contribution. The combined NLO fractions are roughly the same as the LO ones, with basically no difference between the additive and multiplicative approaches.

JHEP10(2021)097

mode	LO	NLO_{EW}	NLO_{QCD}	gg	NLO_{+}	$\text{NLO}_{\times}$
unpol.	100%	100%	100%	100%	100%	100%
$\text{Z}_\text{L}\text{Z}_\text{L}$	5.8%	5.9%	5.9%	5.4%	5.8%	5.8%
$\text{Z}_\text{L}\text{Z}_\text{T}$	11.8%	11.9%	12.7%	2.1%	11.7%	11.6%
$\text{Z}_\text{T}\text{Z}_\text{L}$	11.9%	12.0%	12.6%	2.1%	11.6%	11.6%
$\text{Z}_\text{T}\text{Z}_\text{T}$	69.3%	69.1%	67.4%	90.4%	69.7%	69.8%
interf.	1.1%	1.1%	1.3%	−0.02%	1.2%	1.2%

Table 4. Polarization fractions in the fiducial setup (see section 2.5) for ZZ production at the LHC at LO and NLO accuracy, shown as percentages relative to the DPA unpolarized result. Polarizations are defined in the CM frame.

We now present differential results in the fiducial region for observables that are relevant for the discrimination among polarization states of the Z bosons using the multiplicative combination of EW and QCD corrections [eq. (3.4)]. We have checked numerically that the corresponding differential results obtained with the additive prescription [eq. (3.3)] are very similar. Non-negligible differences between the two approaches only appear in phase-space regions where the cross-section for ZZ production is suppressed. While the multiplicative combination of NLO corrections is theoretically preferable over the additive one, it causes artificial effects in phase-space regions where the LO cross-section is suppressed, particularly for the LL polarization state. In figures 9–17 we focus on the size of interferences, on the relative impact of higher-order corrections, and on the differences among the shapes of polarized distributions.

As first observable we consider the transverse momentum of the electron-positron system in figure 9. In the case of DPA calculations, this observable coincides with the transverse momentum of the Z boson that decays into the two dressed leptons e^+ and e^-. In the soft region of the spectrum, the non-doubly-resonant background (the deviation of the grey curves from 1 in the left middle panel) contributes 6% (4%) to the full result at LO ($\text{NLO}_\times$). In the same kinematic region, the interferences (the difference between the grey and magenta curves in the left middle panel) range between 2% and 3%, while they are below the 1% level at moderate and large transverse momenta. The unpolarized distribution is dominated by the TT polarization mode both at LO and when including radiative corrections. The LL and LT polarized distributions are strongly suppressed at large transverse momenta, where they are two orders of magnitude smaller than the unpolarized and purely-transverse ones, while the TL mode is only suppressed by one order of magnitude. The LL polarization state, which is strongly suppressed at LO w.r.t. to all other polarization states, receives a sizeable enhancement from QCD real corrections and loop-induced contributions, already at moderate transverse momentum. The two mixed-polarization distributions have similar behaviours for $p_{\text{T,e}^+\text{e}^-} \lesssim 100\,\text{GeV}$, while at larger values the TL mode receives huge (up to 1000%) corrections from real QCD radiation, mostly coming from the gq, $g\bar{q}$ partonic processes that open up at NLO QCD. In the TL

JHEP10(2021)097

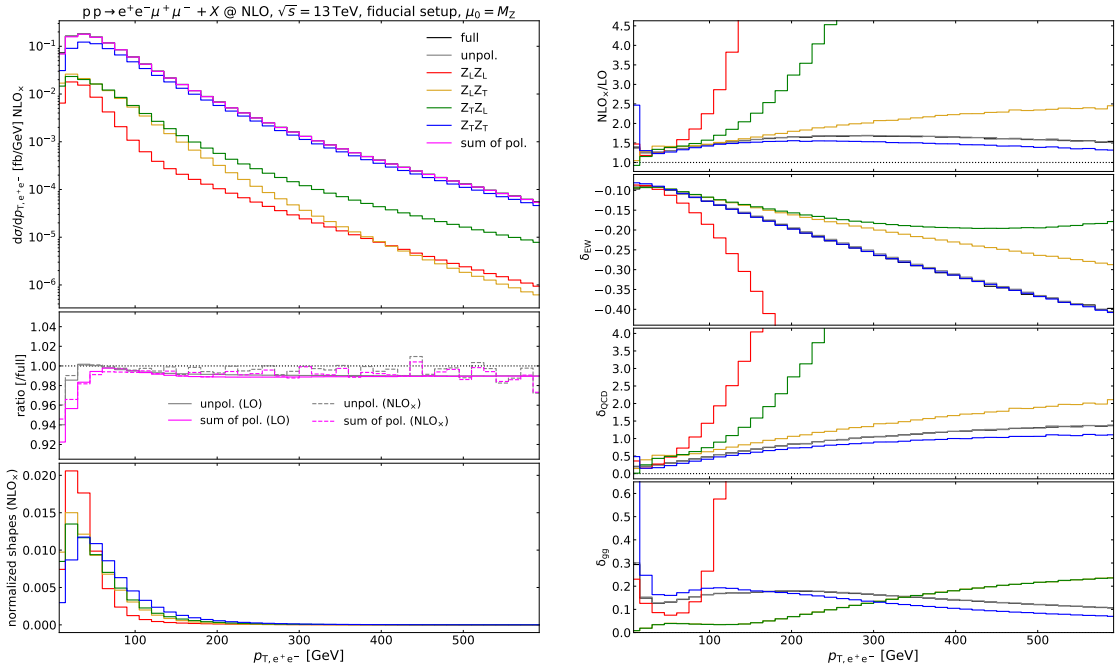

Figure 9. Distributions in the transverse momentum of the e^+e^- system. Unpolarized and doubly-polarized results are shown for ZZ production at the LHC in the fiducial setup described in section 2.5 with polarizations defined the CM frame. Left panel from top down: $NLO_\times$ differential cross-sections, ratios of DPA over the full result, normalized $NLO_\times$ shapes (unit integral). Right panel from top down: $NLO_\times$ K-factor, NLO EW corrections δ_{EW}, NLO QCD correction δ_{QCD}, gg contribution δ_{gg}. All curves in the right panel are relative to the LO cross-sections.

polarization configuration, a large p_T of the transverse boson implies that also the longitudinal boson has large p_T at LO, giving a suppression in the cross-section by $1/p_T^2$ w.r.t. to the TT polarization state. In the presence of QCD radiation, the transverse momentum needed to balance a large p_T of the transverse boson is shared by the longitudinal boson and the radiated gluon or quark. Therefore, the longitudinal Z boson carries smaller p_T than at LO giving a much less severe suppression to the signal. For the LT polarization configuration, on the other hand, the presence of real radiation does not influence the transverse momentum of the longitudinal boson in the considered distribution. The large transverse momentum of the longitudinal Z boson suppresses the contributions at LO and NLO QCD alike. This argument explains a LT signal that is 10 times smaller than the TL one for $p_{T,e^+e^-} \gtrsim 500\,\text{GeV}$ and the enhancement of the LL mode by real QCD radiation. An analogous effect is not present at NLO EW, because the EW virtual corrections are noticeably larger than real ones, the EW coupling is suppressed w.r.t. the QCD case, and the photon-induced partonic processes (γq, $\gamma\bar{q}$) are less luminous than those with a gluon in the initial state. The loop-induced gluon-gluon contributions are particularly sizeable for the TT signal in the very soft region of the spectrum, where the quark-induced LO TT cross-section is suppressed owing to angular-momentum conservation (the soft-p_T region corresponds to a scattering angle that is close to zero or π). Although all polarized

JHEP10(2021)097

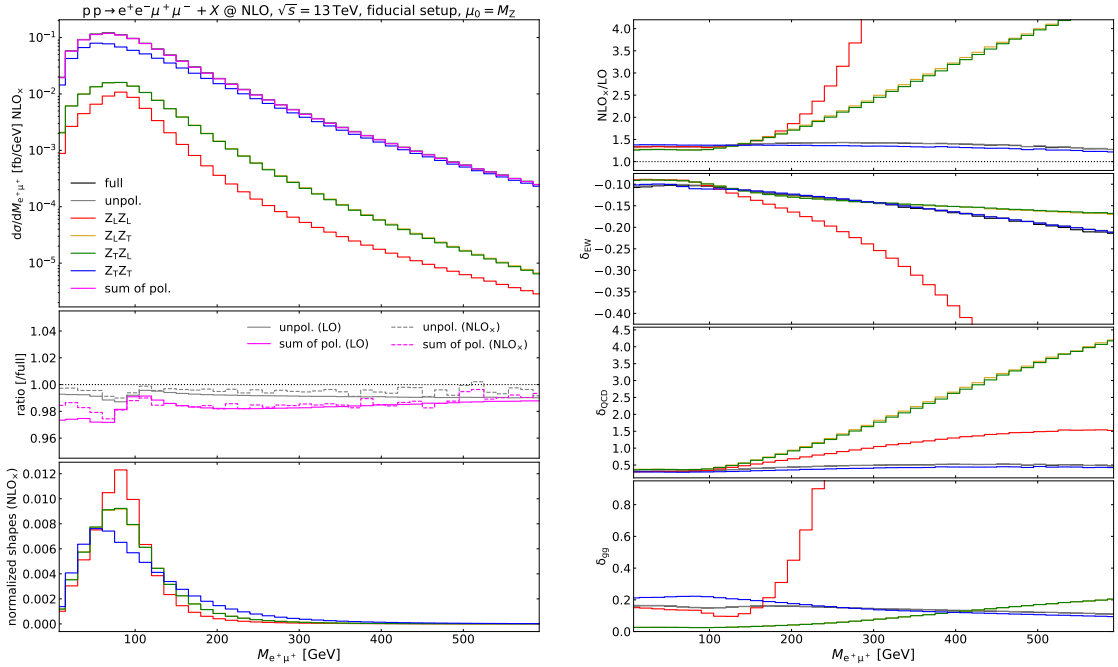

Figure 10. Distributions in the invariant mass of the $e^+\mu^-$ system. Same structure as in figure 9.

distributions are peaked at small transverse momenta, the transverse momentum of a single Z boson is sensitive to the polarization state of both Z bosons thanks to the strong kinematic and spin correlation between the two bosons. In fact, the normalized shape of the LL distribution is much narrower than the TT one, while the normalized shapes of mixed-polarization configurations show an intermediate behaviour between the LL and TT ones. This indicates that the transverse momentum of a single Z boson provides a handle to separate the LL polarization state from the others.

In figure 10, we display the distributions in the invariant mass of the $e^+\mu^+$ pair. This variable shares strong similarities with the invariant mass of the four-lepton system (not shown) concerning relative NLO corrections, but is characterized by an enhanced discrimination power among polarizations. It has been found to be sensitive to polarizations of Z bosons also in Higgs decays [53, 54]. The non-doubly-resonant background is as small as at the integrated level, and the interferences amount to at most 2% of the unpolarized result in the considered range. Although the LL and mixed modes are strongly suppressed w.r.t. the TT mode already at moderate invariant mass, in the soft region of the spectrum the shapes of polarized distributions are different. The TT distribution is characterized by a maximum around 50 GeV and a rather large width, while the maximum of the LL curve is around 80 GeV and the shape is narrower. The results for the mixed states lie in between those of the TT and LL ones. The suppression of the LO distributions for the polarization states with one or two longitudinal bosons at high $M_{e^+\mu^+}$ entails a strong impact of NLO and loop-induced contributions. As observed in invariant-mass and transverse-momentum distributions in the inclusive setup [see figure 8(a)], the EW corrections grow large and negative for the purely-longitudinal signal, accounting for −40% of the LO pre-

JHEP10(2021)097

diction at $M_{e^+\mu^+} \approx 400\,\text{GeV}$, while milder EW corrections are found for other polarization states, ranging between -10% and -20% in the considered range. The QCD corrections are similar to those at the integrated level in the soft region of the spectrum, while for $M_{e^+\mu^+} \gtrsim 100\,\text{GeV}$ the LL and mixed signals are enhanced by very large real-radiation contributions both in the $q\bar{q}$ and in the $gq, g\bar{q}$ partonic channels. The QCD radiative effects are particularly large for the mixed states, resulting in NLO QCD cross-sections that are five times larger than the LO ones at $M_{e^+\mu^+} \approx 600\,\text{GeV}$. This effect is due to huge real contributions from the gluon–(anti)quark channels that enhance the mixed signals more sizeably than the LL one.[2] The purely-longitudinal signal is affected by large gluon-induced contributions that grow fast towards larger invariant masses, where the LO $q\bar{q}$ contributions are highly suppressed. The multiplicative combination of corrections gives huge and monotonically increasing K-factors for the LL state, slightly smaller but still very large K-factors for the mixed states, while the TT and unpolarized results feature decreasing K-factors ($+40\%$ in the soft region, $+25\%$ at $M_{e^+\mu^+} \approx 600\,\text{GeV}$) owing to the negative EW corrections that are also applied to the flat QCD correction, and to the decreasing gluon-induced contribution in the high-energy regime.

Very large effects of higher-order corrections to longitudinal signals are not only found in the tails of invariant-mass and transverse-momentum distributions, but also in inclusive angular variables like the cosine of the scattering angle between the two Z bosons presented in figure 11. The scattering angle $\theta_{V_1}^{\text{CM}}$ is defined as the angle between the momentum of the e^+e^- pair computed in the rest frame of the four-lepton system and the momentum of the four-lepton system computed in the LAB frame. At LO it coincides with the scattering angle between the two Z bosons that is used (for on-shell bosons) in eq. (2.22). At NLO it receives substantial modifications by real-radiation contributions. The interferences are almost vanishing for $\theta_{V_1}^{\text{CM}} = \pi/2$, while they reach the 3% level in the forward and backward regions, where the unpolarized, transverse-transverse and mixed-polarization distributions have their maxima. The peaks in these regions are particularly pronounced for the mixed signals. The LL signal has maxima at slightly more central configurations ($\cos\theta_{V_1}^{\text{CM}} \approx \pm 0.9$). At $\cos\theta_{V_1}^{\text{CM}} = 0$ the polarized signals display a rather different behaviour. The TT signal has a minimum, the mixed states have a local maximum, while the purely-longitudinal distribution is characterized by an impressive enhancement, which is an artificial effect of the multiplicative combination of the NLO corrections. In fact, the LL signal vanishes at $\cos\theta_{V_1}^{\text{CM}} = 0$, while the NLO corrections do not, i.e. the additional term w.r.t. the additive combination ($\Delta\sigma_{\text{EW}}\Delta\sigma_{\text{QCD}}/\sigma_{\text{LO}}$) becomes huge. We have checked that the additive combination gives a smooth LL curve around $\cos\theta_{V_1}^{\text{CM}} = 0$. As a consequence, the multiplicative combination of NLO corrections should be applied with a grain of salt and compared against the results of the additive combination, particularly in those regions where the LO is very small or vanishing. The fake effects of the multiplicative combination at $\cos\theta_{V_1}^{\text{CM}} = 0$ are also present in the K-factor shown in the right top panel of figure 11, while the huge effects in the relative corrections δ_{EW}, δ_{QCD}, and δ_{gg} simply result from the normalisation to the vanishing LO cross-section. Also EW corrections to

[2] This enhancement is not directly related to the suppression of longitudinal polarizations.

JHEP10(2021)097

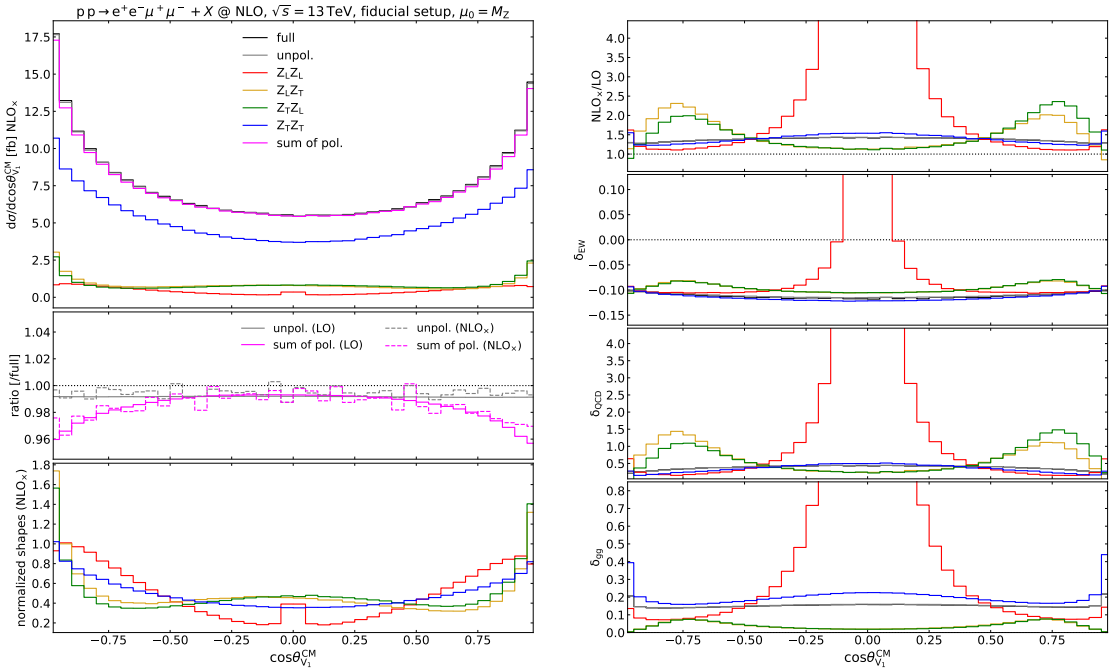

Figure 11. Distributions in the scattering angle of the Z boson decaying into e^+e^- in the four-lepton CM frame computed w.r.t. the four-lepton-system direction in the LAB frame. Same structure as in figure 9.

the LL distribution become large and positive in the central region, while they are negative and flat towards $\cos\theta_{V_1}^{\mathrm{CM}} = \pm 1$. The combined $\mathrm{NLO}_\times$ corrections to the TT distribution are relatively flat, apart from an enhancement in the forward and backward regions due to the gluon-induced contribution. Mixed-polarization distributions receive NLO QCD corrections and gluon-induced contributions that are maximal around $\cos\theta_{V_1}^{\mathrm{CM}} = \pm 0.75$. A similar shape in the relative correction is found also for EW corrections. Up to the effects of the multiplicative combination, the different shapes for the various polarized signals and the rather small interference effects make this angular variable very suitable for the discrimination among polarization states.

The possibility to fully reconstruct the rest frame of each Z boson gives access to the lepton decay angles, which are the most direct probes of the polarization states of decayed bosons. We consider in figure 12 the cosine of the polar decay angle of the positron in the corresponding Z-boson rest frame. The NLO EW distributions in the inclusive setup for the same variable are shown in figure 6(a). The effect of transverse-momentum and rapidity cuts on this observable is mild and restricted to $\cos\theta_{e^+}^{*,\mathrm{CM}} = \pm 1$, where the TT and TL distributions do not have a maximum anymore. The size of interferences is similar to the one found at the integrated level, ranging from 0.3% of the full result in the central region to 2% around $\cos\theta_{e^+}^{*,\mathrm{CM}} \approx \pm 0.7$. This observable is highly sensitive to the polarization of the Z boson that decays to e^+e^-, as can be appreciated from the comparison of normalized shapes for the various polarized signals. There is no shape difference between the LL and LT curves, despite the different cuts applied on the $e^\pm$ and $\mu^\pm$ kinematics, and

JHEP10(2021)097

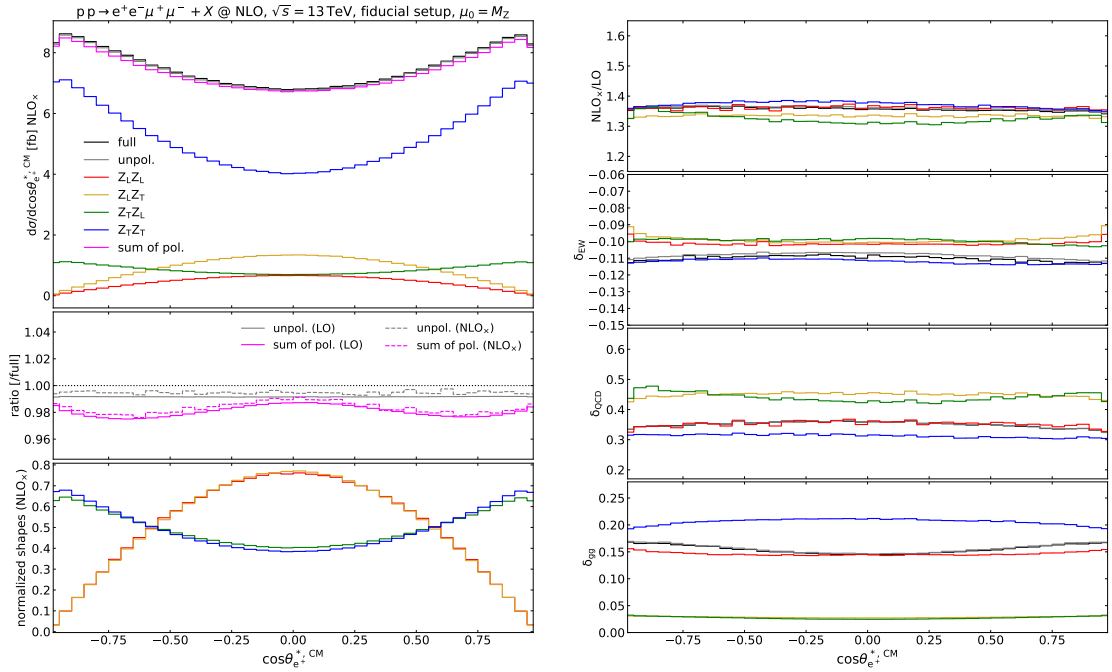

Figure 12. Distributions in the cosine of the polar decay angle of the positron $\theta^{*,\mathrm{CM}}_{\mathrm{e}^+}$ in its corresponding Z-boson rest frame computed w.r.t. the Z-boson spatial direction in the CM frame. Same structure as in figure 9.

very small shape differences are found between the TL and TT curves. Obviously, in order to discriminate between the longitudinal and transverse polarizations of the Z boson decaying into $\mu^+\mu^-$ the $\cos\theta^{*,\mathrm{CM}}_{\mathrm{e}^+}$ variable is not helpful. The distributions are not distorted sizeably by the inclusion of higher-order corrections neither for polarized signals nor for the unpolarized ones. In fact, the NLO effects and the loop-induced contribution entail rather flat corrections to this observable, resulting in combined K-factors that are comparable with those of the integrated results in the whole angular range. Owing to lepton universality, the results for the $\cos\theta^{*,\mathrm{CM}}_{\mu^+}$ variable are very similar to those for $\cos\theta^{*,\mathrm{CM}}_{\mathrm{e}^+}$ up to small effects due to the different transverse-momentum and rapidity cuts for the two lepton flavours.

It is clear that any experimental analysis that targets the polarization of Z bosons should rely on decay angles as discriminating variables. In the rest frame of a single Z boson, the leptonic-decay kinematics is fully described by the polar decay angle, $\theta^{*,\mathrm{CM}}_{\ell^+}$, and the azimuthal one, $\phi^{*,\mathrm{CM}}_{\ell^+}$. If two Z bosons are produced, it is interesting to investigate the spin correlation between them by means of the difference between azimuthal decay angles of the positively-charged leptons, each computed in the corresponding Z-boson rest frame. This variable has been proved to be sensitive to the polarization of weak bosons that come from a Higgs decay [53, 54]. Since polarizations are defined in the CM frame, the reference direction for the angle $\phi^{*,\mathrm{CM}}_{\mathrm{e}^+}$ coincides with the one for $\phi^{*,\mathrm{CM}}_{\mu^+}$, up to a minus sign, and both angles are measured relative to the same plane. The azimuthal difference

JHEP10(2021)097

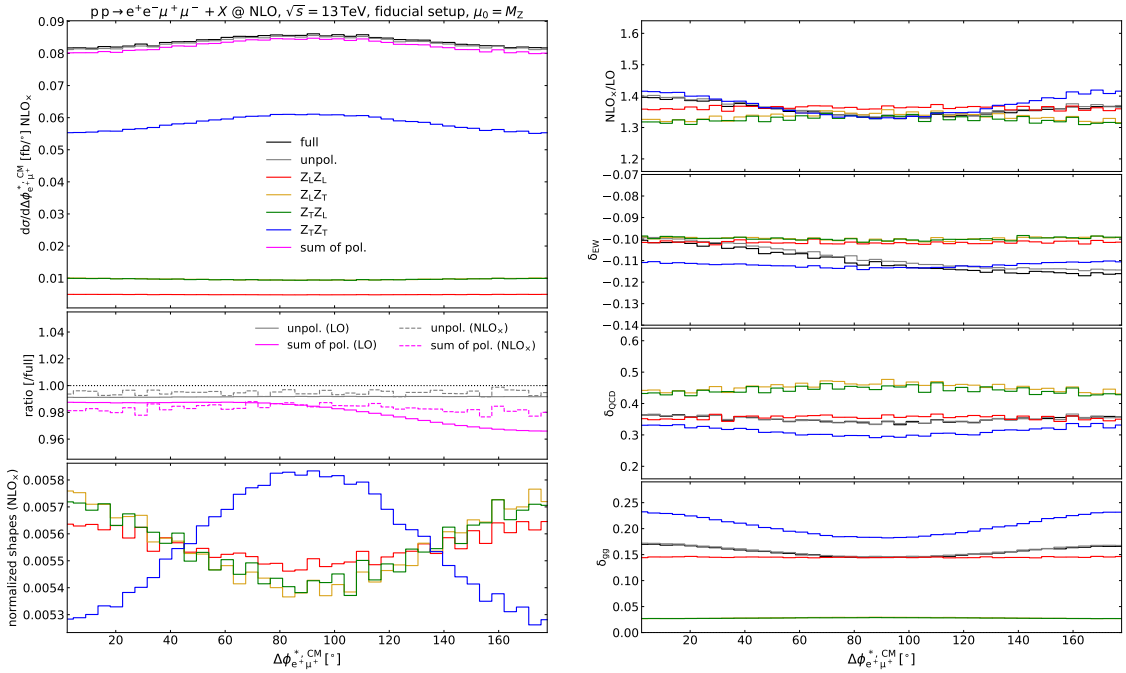

Figure 13. Distributions in the difference between azimuthal decay angles $\phi_{e^+}^{*,\mathrm{CM}}$ and $\phi_{\mu^+}^{*,\mathrm{CM}}$, where $\phi_{\ell^+}^{*,\mathrm{CM}}$ is the decay angle of the positively-charged lepton in its corresponding Z-boson rest frame computed w.r.t. the Z-boson spatial direction in the CM frame. Same structure as in figure 9.

is defined as

$$\Delta\phi_{e^+\mu^+}^{*,\mathrm{CM}} = \min\left(\left|\phi_{e^+}^{*,\mathrm{CM}} - \phi_{\mu^+}^{*,\mathrm{CM}}\right|,\, 2\pi - \left|\phi_{e^+}^{*,\mathrm{CM}} - \phi_{\mu^+}^{*,\mathrm{CM}}\right|\right), \tag{3.6}$$

and the distributions in this variable are shown in figure 13. The polarized and unpolarized distributions are symmetric about $\Delta\phi_{e^+\mu^+}^{*,\mathrm{CM}} = \pi/2$, and the non-doubly-resonant background reflects the integrated results with no shape distortion. The interferences vary between 0.5% and 3% at LO, showing a sizeable increase towards $\Delta\phi_{e^+\mu^+}^{*,\mathrm{CM}} = \pi$. On the contrary, the combined NLO results give rather constant interference effects over the whole angular range. The QCD corrections are pretty flat for all polarized and unpolarized signals, while a noticeable shape difference is found between LO and loop-induced results for the TT signal. The EW radiative corrections are constant for polarized signals, while a 1.5% variation shows up in the relative correction for the unpolarized case, which is due to the different interference patterns at LO and at NLO EW. While an 8% variation is found in the combined K-factor for the TT signal, the variations for signals with one or two longitudinal bosons are much smaller. The comparison of normalized shapes demonstrates that this variable is particularly suitable for the separation of the TT polarization mode. In fact, the distribution for this mode has a maximum at $\Delta\phi_{e^+\mu^+}^{*,\mathrm{CM}} = \pi/2$ and minima at $\Delta\phi_{e^+\mu^+}^{*,\mathrm{CM}} = 0, \pi$, while the other modes exhibit the opposite behaviour. Furthermore, the LL and mixed distributions are somewhat flatter than the TT one. Separating the purely-longitudinal state from the mixed ones is less straightforward with this observable, as the shape differences among these modes are mild.

JHEP10(2021)097

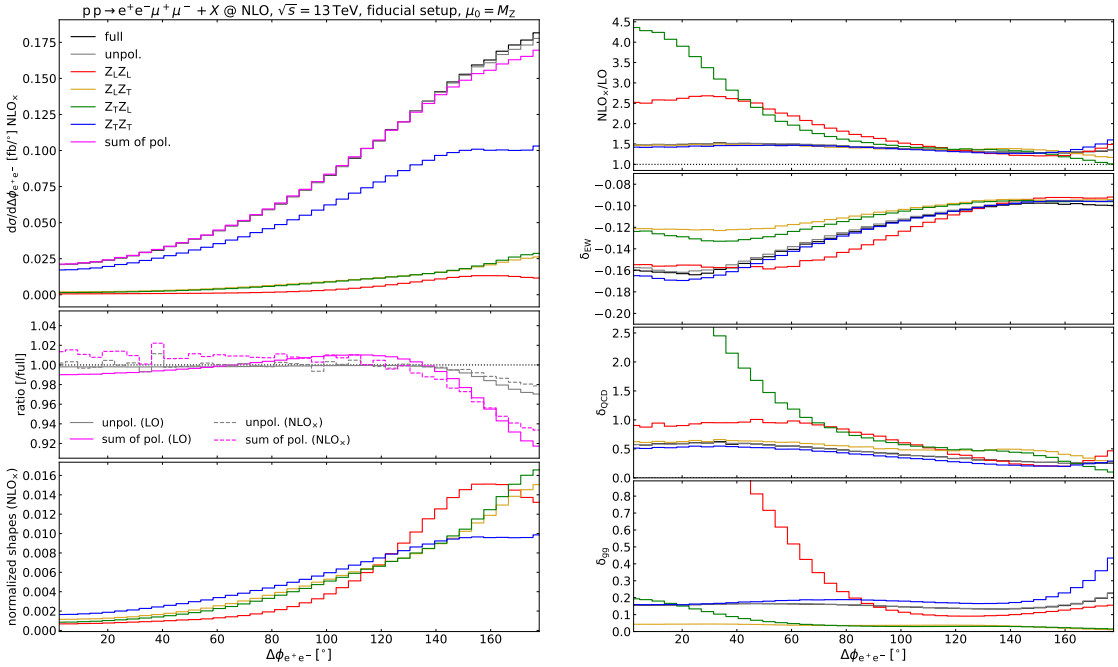

Figure 14. Distributions in the azimuthal separation between the positron and the electron. Same structure as in figure 9.

Also other angular variables are sensitive to the polarization of Z bosons. In figure 14 we present the differential distributions in the azimuthal separation (computed in the LAB frame) between the positron and the electron. In the DPA calculations, either polarized or unpolarized, the two leptons are decay products of a Z boson and are typically produced in opposite hemispheres. The non-doubly-resonant effects are compatible with zero in most of the spectrum of this observable, while they get slightly larger in the most populated region, reaching 2.5% and 2% at LO and at $\text{NLO}_\times$, respectively. Around $\Delta\phi_{\text{e}^+\text{e}^-} = \pi$ also large interferences show up, contributing up to 5% to the full results, both in LO and in $\text{NLO}_\times$ predictions. The NLO EW corrections are at the -10% level in the most populated region, while they become more sizeable at $\Delta\phi_{\text{e}^+\text{e}^-} = 0$ (-16% for diagonal polarization states, -12% for mixed ones). Huge QCD corrections (more than 300%) are found for the TL signal in the regime of small azimuthal separation, which result from real corrections, in particular from those with initial-state gluons. The QCD corrections are smaller, but still large, for the LL signal (around 100%), while for other polarized and for the unpolarized signals QCD corrections never exceed 60% in the whole range. Large gluon-induced contributions to the purely-longitudinal signal are found for $\Delta\phi_{\text{e}^+\text{e}^-} < \pi/2$. The combination of all corrections gives large K-factors for the TL signal (up to 4.5) and to the LL one (up to 2.7). The comparison of polarized signals reveals different distribution shapes, with monotonically-increasing curves for the mixed states, a plateau in the region $\Delta\phi_{\text{e}^+\text{e}^-} > 5\pi/6$ for the TT state, and a maximum near $\Delta\phi_{\text{e}^+\text{e}^-} = 8\pi/9$ for the LL state. This renders this observable suitable for the discrimination among polarization modes in LHC data, provided that also the interference contribution and the irreducible background are properly accounted for in a SM-template fit of the data.

JHEP10(2021)097

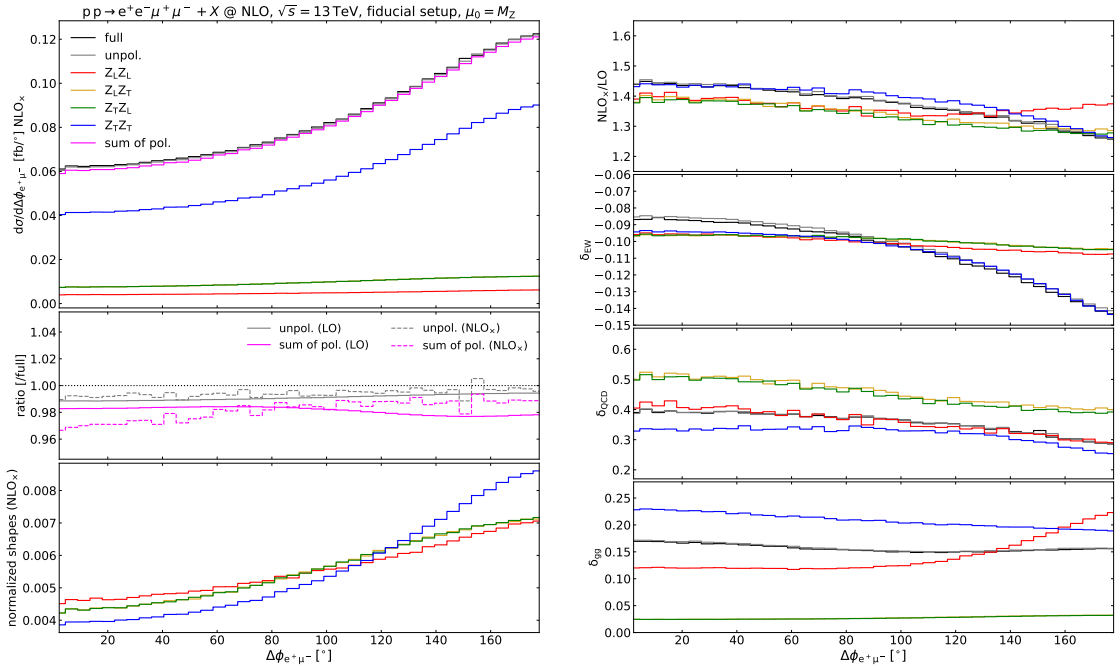

Figure 15. Distributions in the azimuthal separation between the positron and the muon. Same structure as in figure 9.

Another variable that is suitable for the polarization discrimination is the azimuthal separation between the positron and the muon considered in figure 15. Since the two particles originate from different Z-boson decays, the distributions are less peaked at π than the $\Delta\phi_{e^+e^-}$ ones. Both LO and combined NLO results give positive interferences ranging between 1% and 2% of the full distribution in the whole angular range. The NLO EW corrections cause sizeable distortions only to the TT polarization mode, as already observed in the inclusive setup [see figure 7(a)]. The impact of QCD corrections diminishes monotonically towards the most populated region, with a 10% variation for the LL and mixed signals and a slightly smaller for the TT one. The gluon-induced process enhances the LO distributions in a rather uniform way for most polarization modes, apart from a 10% increase for the LL mode. The combined NLO distributions suggest that this angular variable is suitable for the separation of the TT signal from the others. In fact, at the level of normalized shapes, the TT curve increases by 100% going from $\Delta\phi_{e^+\mu^-} = 0$ to $\Delta\phi_{e^+\mu^-} = \pi$, while other polarized curves increase by roughly 50% only.

In figure 16 we present the distributions in the rapidity of the electron-positron system. Owing to the selection cut on the rapidities of both e^+ and e^-, $|y_{e^\pm}| < 2.47$, also the combination of the two momenta, i.e. the reconstructed Z boson, is central. The non-doubly-resonant effects are flat and equal to those in the total cross-section. A positive 3.5% interference contribution appears in the most forward and backward configurations allowed by the selections, while in the central region, which is the most populated one, the interferences account for less than 1%. The EW corrections are pretty flat for all polarization modes, while some distortions of the LO curves are introduced by QCD corrections

JHEP10(2021)097

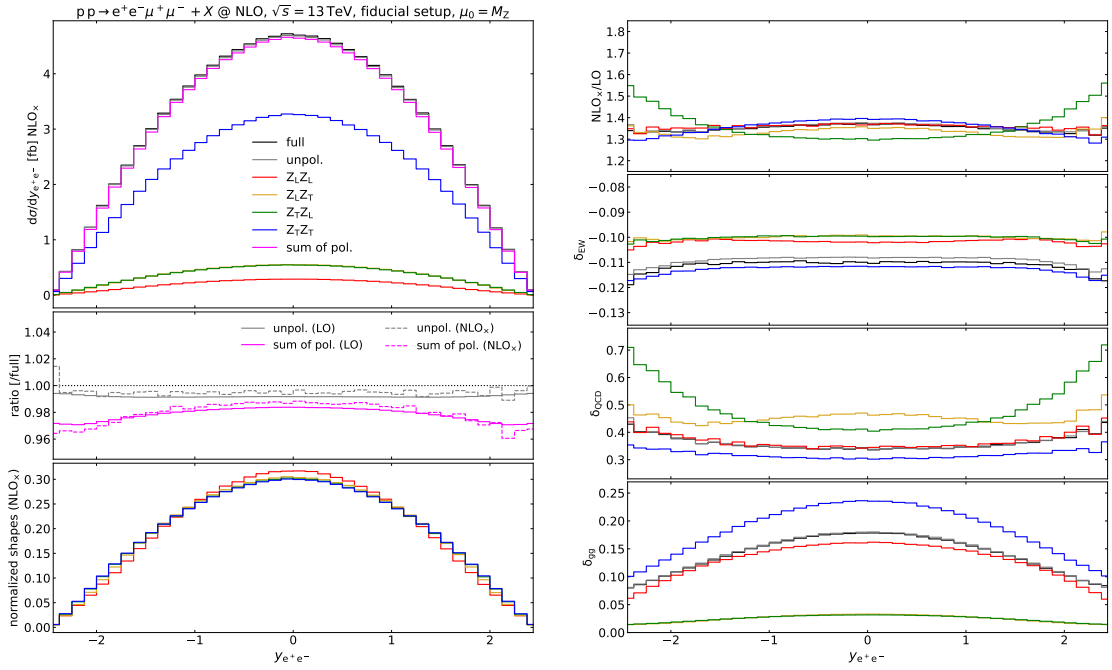

Figure 16. Distributions in the rapidity of the e^+e^- pair (single Z boson). Same structure as in figure 9.

and by loop-induced contributions. The NLO QCD corrections enhance in particular the TL distribution by up to 70% in the most forward and backward regions, while milder effects are found for other polarization states. The loop-induced contributions sizeably enhance the LL and the TT distributions, with maximal effects in the central region (23% for TT, 15% for LL, at $y_{e^+e^-} = 0$). The multiplicative combination of corrections results in K-factors varying between 1.3 and 1.4 (with a similar pattern) for all polarized signals but the TL one, which varies from 1.3 in the central region to 1.55 in the most forward and backward regions. All combined distributions have a maximum at zero rapidity, and are characterized by a negative convexity in the whole available range, with very small shape differences among different polarization states. This shows that the rapidity of a single Z boson is hardly sensitive to the polarization of the decayed boson, as it has been already found in WZ production with polarizations defined in the di-boson CM frame [80].

Finally, we consider distributions in the absolute value of the rapidity separation between the two Z bosons in figure 17. The momenta of the Z bosons are determined from the momenta of their decay products after possible photon recombination. Owing to the rapidity cuts on all charged leptons, the rapidity distance between the two opposite-flavour lepton pairs is implicitly cut such that $|\Delta y_{ZZ}| \lesssim 5$, but already at $|\Delta y_{ZZ}| \approx 4$ all cross-sections are more than 3 orders of magnitude lower than those at the maximum of the distributions. The region of small rapidity separation is the most populated one for all polarized and unpolarized signals. In this configuration, the events are characterized by slightly larger non-doubly-resonant effects (2%) than those found at the integrated level, and by almost vanishing interferences, both at LO and at NLO. For larger rapidity sepa-

JHEP10(2021)097

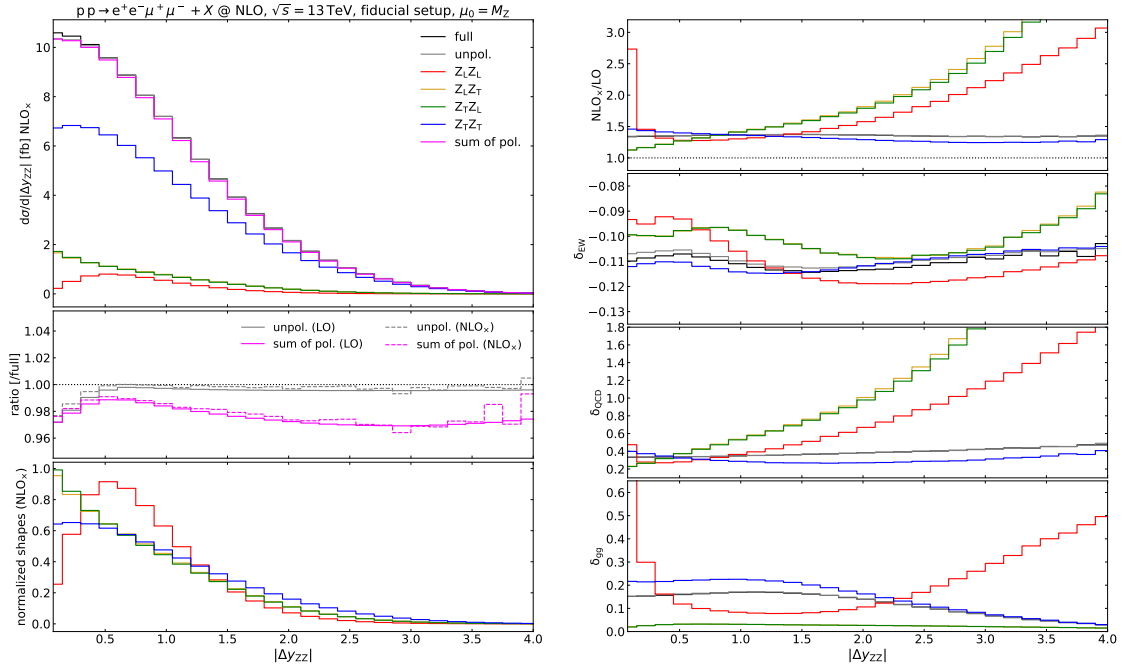

Figure 17. Distributions in the absolute value of the rapidity separation between the two Z bosons. Same structure as in figure 9.

rations, the non-doubly-resonant background becomes smaller than 0.5% of the full result, while interferences increase up to 3%. The NLO EW corrections, despite the different patterns for various polarization modes, induce only mild shape distortions of the distributions with at most 3% variations in the considered range for the LL and mixed polarization states. Even flatter EW corrections are found for the purely-transverse and for the unpolarized distributions. At variance with the EW effects, the NLO QCD corrections sizeably increase from small to large rapidity separations for the LL and mixed polarization states reaching 120% and 180%, respectively, at $|\Delta y_{ZZ}| = 3$. A 50% enhancement results for the LL state at zero rapidity separation, due to the fact that this polarization state is strongly suppressed in such configuration at LO. The QCD corrections for the purely-transverse state turn out to be relatively flat. The loop-induced process enhances the suppressed LO cross-section with both longitudinally-polarized bosons by 150% at $|\Delta y_{ZZ}| \approx 0$ and causes effects of up to 50% for large rapidity separations for the same polarization mode. About 20% loop-induced contributions characterize the TT signal at small rapidity separation. The normalized TT distribution has a flat maximum at $|\Delta y_{ZZ}| \approx 0.2$, while mixed contributions have pronounced maxima at zero rapidity separation. The LL distribution is maximal at $|\Delta y_{ZZ}| \approx 0.5$ with a shape that is noticeably different from the other three polarization states. Therefore, using this observable in a fit to LHC data is expected to improve the capability of isolating the purely-longitudinal signal from the other ones.

JHEP10(2021)097

4 Conclusion

Extending the methods of refs. [79, 80] to NLO EW corrections and in particular to the emission of photons off the decay products of Z bosons, we have presented a general procedure to compute cross-sections for the production of Z bosons in definite polarization states valid up to NLO accuracy both in the EW and in the QCD coupling. The definition of polarized signals relies on the application of a double-pole approximation (DPA) to contributions with two resonant Z bosons and on the separation of polarization states at the amplitude level. While the method is applicable to any LHC process with neutral resonances, even including identical particles in the final state, we have focused on inclusive Z-pair production in the different-flavour four-charged-lepton channel at complete NLO accuracy, including also gluon-initiated, loop-induced contributions.

We have first applied the newly-introduced DPA techniques to the unpolarized process at NLO EW for very inclusive selection cuts, finding a small contribution ($\approx 1\%$) of the non-doubly-resonant background to the full computation. Beyond its phenomenological importance, this result provides a validation of the DPA method for complete NLO corrections, and in particular of the well-behaved definition of subtraction counterterms that are needed for the cancellation of IR singularities in the DPA calculation.

In the same inclusive setup, the separation of polarizations for both Z bosons has been investigated, comparing the results of two different definitions of polarization vectors, one in the di-boson centre-of-mass (CM) frame and one in the laboratory (LAB) frame. Despite the absence of cuts on single leptons, non-negligible interference patterns are found in some differential distributions both at LO and at NLO EW. Sizeable differences show up between the CM- and LAB-frame definitions of polarizations, but smaller interference effects are present when defining the polarizations in the CM frame, which is also more natural for ZZ production.

In the presence of realistic fiducial cuts, inspired by the latest ATLAS analysis, we have combined NLO EW and QCD corrections and gluon-induced contributions (formally of NNLO QCD accuracy) both in a multiplicative and in an additive way. While the multiplicative combination is better motivated from the theory point of view in general, it introduces artificial effects in regions of phase space where the purely-longitudinal signal is suppressed at LO.

Scale uncertainties are at the 5% level in the combined NLO predictions both for unpolarized and polarized signals. A substantial fraction of the NLO scale uncertainties is due to the gluon-induced process, in particular for the polarization modes with equally polarized Z bosons (transverse-transverse and longitudinal-longitudinal).

In spite of sizeable and negative EW corrections of about -10%, the largest radiative effects originate from NLO QCD corrections which cause an increase of the LO cross-section of about 35%. Also the gluon-induced process contributes noticeably to ZZ production ($\approx$ 15–20% for unpolarized ZZ pairs and those with equal polarizations). Polarization fractions are roughly conserved going from LO to NLO accuracy, but sizeable distortions are found at the differential level with rather different K-factors for the various polarization states.

JHEP10(2021)097

At variance with di-boson processes with neutrinos as decay products, the possibility to fully reconstruct the final state allows for access to a large set of observables. We have presented a number of differential results for fiducial event selections, focusing on those variables that are particularly suited for the separation of polarized signals. The non-doubly-resonant background (0.5% at the integrated level) never exceeds 3% of the full result for all presented differential distributions. Interferences, which are at the 1% level in the integrated cross-section, can reach up to 5% in more exclusive phase-space regions. Several angular variables, including decay angles as well as azimuthal and rapidity separations are well suited for polarization discrimination. However, also some invariant-mass distributions show a fair discrimination power among different polarization states. A combination of the variables considered in this paper, either in a multivariate analysis or as input to machine-learning techniques, is expected to allow for the separation of polarized states in the LHC data despite the small rate of the unpolarized process and the strongly-suppressed cross-section for longitudinal bosons.

Acknowledgments

We thank Jean-Nicolas Lang for supporting Recola and Mathieu Pellen for help with MoCaNLO. GP thanks Alessandro Ballestrero and Ezio Maina for useful discussion. The authors acknowledge financial support by the German Federal Ministry for Education and Research (BMBF) under contract no. 05H18WWCA1.

References

[1] ATLAS collaboration, *Constraints on off-shell Higgs boson production and the Higgs boson total width in $ZZ \to 4\ell$ and $ZZ \to 2\ell 2\nu$ final states with the ATLAS detector*, *Phys. Lett. B* **786** (2018) 223 [arXiv:1808.01191] [INSPIRE].

[2] CMS collaboration, *Measurements of the Higgs boson width and anomalous HVV couplings from on-shell and off-shell production in the four-lepton final state*, *Phys. Rev. D* **99** (2019) 112003 [arXiv:1901.00174] [INSPIRE].

[3] CMS collaboration, *Constraints on anomalous Higgs boson couplings using production and decay information in the four-lepton final state*, *Phys. Lett. B* **775** (2017) 1 [arXiv:1707.00541] [INSPIRE].

[4] ATLAS collaboration, *Measurements of the Higgs boson inclusive and differential fiducial cross sections in the 4ℓ decay channel at $\sqrt{s} = 13$ TeV*, *Eur. Phys. J. C* **80** (2020) 942 [arXiv:2004.03969] [INSPIRE].

[5] CMS collaboration, *Measurement of the ZZ production cross section and $Z \to \ell^+\ell^-\ell'^+\ell'^-$ branching fraction in pp collisions at $\sqrt{s} = 13$ TeV*, *Phys. Lett. B* **763** (2016) 280 [*Erratum ibid.* **772** (2017) 884] [arXiv:1607.08834] [INSPIRE].

JHEP10(2021)097

[6] CMS collaboration, *Measurements of the* pp → ZZ *production cross section and the* Z → 4ℓ *branching fraction, and constraints on anomalous triple gauge couplings at* $\sqrt{s} = 13$ *TeV*, *Eur. Phys. J. C* **78** (2018) 165 [*Erratum ibid.* **78** (2018) 515] [arXiv:1709.08601] [INSPIRE].

[7] ATLAS collaboration, *$ZZ \to \ell^+\ell^-\ell'^+\ell'^-$ cross-section measurements and search for anomalous triple gauge couplings in 13 TeV pp collisions with the ATLAS detector*, *Phys. Rev. D* **97** (2018) 032005 [arXiv:1709.07703] [INSPIRE].

[8] CMS collaboration, *Measurements of* pp → ZZ *production cross sections and constraints on anomalous triple gauge couplings at* $\sqrt{s} = 13$ *TeV*, *Eur. Phys. J. C* **81** (2021) 200 [arXiv:2009.01186] [INSPIRE].

[9] ATLAS collaboration, *Measurement of the four-lepton invariant mass spectrum in 13 TeV proton-proton collisions with the ATLAS detector*, *JHEP* **04** (2019) 048 [arXiv:1902.05892] [INSPIRE].

[10] ATLAS collaboration, *Measurements of differential cross-sections in four-lepton events in 13 TeV proton-proton collisions with the ATLAS detector*, *JHEP* **07** (2021) 005 [arXiv:2103.01918] [INSPIRE].

[11] B. Mele, P. Nason and G. Ridolfi, *QCD radiative corrections to Z boson pair production in hadronic collisions*, *Nucl. Phys. B* **357** (1991) 409 [INSPIRE].

[12] J. Ohnemus and J.F. Owens, *An Order α_s calculation of hadronic ZZ production*, *Phys. Rev. D* **43** (1991) 3626 [INSPIRE].

[13] J. Ohnemus, *Hadronic ZZ, W^-W^+, and $W^\pm Z$ production with QCD corrections and leptonic decays*, *Phys. Rev. D* **50** (1994) 1931 [hep-ph/9403331] [INSPIRE].

[14] L.J. Dixon, Z. Kunszt and A. Signer, *Helicity amplitudes for $O(\alpha_s)$ production of W^+W^-, $W^\pm Z$, ZZ, $W^\pm\gamma$, or $Z\gamma$ pairs at hadron colliders*, *Nucl. Phys. B* **531** (1998) 3 [hep-ph/9803250] [INSPIRE].

[15] L.J. Dixon, Z. Kunszt and A. Signer, *Vector boson pair production in hadronic collisions at order α_s: Lepton correlations and anomalous couplings*, *Phys. Rev. D* **60** (1999) 114037 [hep-ph/9907305] [INSPIRE].

[16] E. Accomando, A. Denner and A. Kaiser, *Logarithmic electroweak corrections to gauge-boson pair production at the LHC*, *Nucl. Phys. B* **706** (2005) 325 [hep-ph/0409247] [INSPIRE].

[17] A. Bierweiler, T. Kasprzik and J.H. Kühn, *Vector-boson pair production at the LHC to $\mathcal{O}(\alpha^3)$ accuracy*, *JHEP* **12** (2013) 071 [arXiv:1305.5402] [INSPIRE].

[18] B. Biedermann, A. Denner, S. Dittmaier, L. Hofer and B. Jäger, *Electroweak corrections to $pp \to \mu^+\mu^-e^+e^- + X$ at the LHC: a Higgs background study*, *Phys. Rev. Lett.* **116** (2016) 161803 [arXiv:1601.07787] [INSPIRE].

[19] B. Biedermann, A. Denner, S. Dittmaier, L. Hofer and B. Jäger, *Next-to-leading-order electroweak corrections to the production of four charged leptons at the LHC*, *JHEP* **01** (2017) 033 [arXiv:1611.05338] [INSPIRE].

[20] J. Baglio, L.D. Ninh and M.M. Weber, *Massive gauge boson pair production at the LHC: a next-to-leading order story*, *Phys. Rev. D* **88** (2013) 113005 [*Erratum ibid.* **94** (2016) 099902] [arXiv:1307.4331] [INSPIRE].

JHEP10(2021)097

[21] S. Kallweit, J.M. Lindert, S. Pozzorini and M. Schönherr, *NLO QCD+EW predictions for $2\ell 2\nu$ diboson signatures at the LHC*, *JHEP* **11** (2017) 120 [arXiv:1705.00598] [INSPIRE].

[22] M. Chiesa, A. Denner and J.-N. Lang, *Anomalous triple-gauge-boson interactions in vector-boson pair production with RECOLA2*, *Eur. Phys. J. C* **78** (2018) 467 [arXiv:1804.01477] [INSPIRE].

[23] F. Cascioli et al., *ZZ production at hadron colliders in NNLO QCD*, *Phys. Lett. B* **735** (2014) 311 [arXiv:1405.2219] [INSPIRE].

[24] M. Grazzini, S. Kallweit and D. Rathlev, *ZZ production at the LHC: fiducial cross sections and distributions in NNLO QCD*, *Phys. Lett. B* **750** (2015) 407 [arXiv:1507.06257] [INSPIRE].

[25] G. Heinrich, S. Jahn, S.P. Jones, M. Kerner and J. Pires, *NNLO predictions for Z-boson pair production at the LHC*, *JHEP* **03** (2018) 142 [arXiv:1710.06294] [INSPIRE].

[26] S. Kallweit and M. Wiesemann, *ZZ production at the LHC: NNLO predictions for $2\ell 2\nu$ and 4ℓ signatures*, *Phys. Lett. B* **786** (2018) 382 [arXiv:1806.05941] [INSPIRE].

[27] F. Caola, K. Melnikov, R. Röntsch and L. Tancredi, *QCD corrections to ZZ production in gluon fusion at the LHC*, *Phys. Rev. D* **92** (2015) 094028 [arXiv:1509.06734] [INSPIRE].

[28] F. Caola, M. Dowling, K. Melnikov, R. Röntsch and L. Tancredi, *QCD corrections to vector boson pair production in gluon fusion including interference effects with off-shell Higgs at the LHC*, *JHEP* **07** (2016) 087 [arXiv:1605.04610] [INSPIRE].

[29] M. Grazzini, S. Kallweit, M. Wiesemann and J.Y. Yook, *ZZ production at the LHC: NLO QCD corrections to the loop-induced gluon fusion channel*, *JHEP* **03** (2019) 070 [arXiv:1811.09593] [INSPIRE].

[30] M. Grazzini, S. Kallweit, M. Wiesemann and J.Y. Yook, *Four lepton production in gluon fusion: Off-shell Higgs effects in NLO QCD*, *Phys. Lett. B* **819** (2021) 136465 [arXiv:2102.08344] [INSPIRE].

[31] M. Grazzini, S. Kallweit, J.M. Lindert, S. Pozzorini and M. Wiesemann, *NNLO QCD + NLO EW with Matrix+OpenLoops: precise predictions for vector-boson pair production*, *JHEP* **02** (2020) 087 [arXiv:1912.00068] [INSPIRE].

[32] T. Melia, P. Nason, R. Röntsch and G. Zanderighi, *W^+W^-, WZ and ZZ production in the POWHEG BOX*, *JHEP* **11** (2011) 078 [arXiv:1107.5051] [INSPIRE].

[33] P. Nason and G. Zanderighi, *W^+W^-, WZ and ZZ production in the POWHEG-BOX-V2*, *Eur. Phys. J. C* **74** (2014) 2702 [arXiv:1311.1365] [INSPIRE].

[34] S. Alioli, F. Caola, G. Luisoni and R. Röntsch, *ZZ production in gluon fusion at NLO matched to parton-shower*, *Phys. Rev. D* **95** (2017) 034042 [arXiv:1609.09719] [INSPIRE].

[35] S. Alioli, S. Ferrario Ravasio, J.M. Lindert and R. Röntsch, *Four-lepton production in gluon fusion at NLO matched to parton showers*, *Eur. Phys. J. C* **81** (2021) 687 [arXiv:2102.07783] [INSPIRE].

[36] M. Chiesa, C. Oleari and E. Re, *NLO QCD+NLO EW corrections to diboson production matched to parton shower*, *Eur. Phys. J. C* **80** (2020) 849 [arXiv:2005.12146] [INSPIRE].

[37] S. Alioli et al., *Next-to-next-to-leading order event generation for Z boson pair production matched to parton shower*, *Phys. Lett. B* **818** (2021) 136380 [arXiv:2103.01214] [INSPIRE].

JHEP10(2021)097

[38] A. Soni and R.M. Xu, *Probing CP-violation via Higgs decays to four leptons*, Phys. Rev. D **48** (1993) 5259 [hep-ph/9301225] [INSPIRE].

[39] D. Chang, W.-Y. Keung and I. Phillips, *CP-odd correlation in the decay of neutral Higgs boson into ZZ, W^+W^-, or $t\bar{t}$*, Phys. Rev. D **48** (1993) 3225 [hep-ph/9303226] [INSPIRE].

[40] A. Skjold and P. Osland, *Angular and energy correlations in Higgs decay*, Phys. Lett. B **311** (1993) 261 [hep-ph/9303294] [INSPIRE].

[41] T. Arens and L.M. Sehgal, *Energy spectra and energy correlations in the decay $H \to ZZ \to \mu^+\mu^-\mu^+\mu^-$*, Z. Phys. C **66** (1995) 89 [hep-ph/9409396] [INSPIRE].

[42] C.P. Buszello, I. Fleck, P. Marquard and J.J. van der Bij, *Prospective analysis of spin- and CP-sensitive variables in $H \to ZZ \to l_1^+l_1^-l_2^+l_2^-$ at the LHC*, Eur. Phys. J. C **32** (2004) 209 [hep-ph/0212396] [INSPIRE].

[43] S.Y. Choi, D.J. Miller, M.M. Mühlleitner and P.M. Zerwas, *Identifying the Higgs spin and parity in decays to Z pairs*, Phys. Lett. B **553** (2003) 61 [hep-ph/0210077] [INSPIRE].

[44] S. Berge, S. Groote, J.G. Körner and L. Kaldamäe, *Lepton-mass effects in the decays $H \to ZZ^* \to \ell^+\ell^-\tau^+\tau^-$ and $H \to WW^* \to \ell\nu\tau\nu_\tau$*, Phys. Rev. D **92** (2015) 033001 [arXiv:1505.06568] [INSPIRE].

[45] K. Hagiwara, Q. Li and K. Mawatari, *Jet angular correlation in vector-boson fusion processes at hadron colliders*, JHEP **07** (2009) 101 [arXiv:0905.4314] [INSPIRE].

[46] Y. Gao, A.V. Gritsan, Z. Guo, K. Melnikov, M. Schulze and N.V. Tran, *Spin Determination of Single-Produced Resonances at Hadron Colliders*, Phys. Rev. D **81** (2010) 075022 [arXiv:1001.3396] [INSPIRE].

[47] S. Bolognesi et al., *On the spin and parity of a single-produced resonance at the LHC*, Phys. Rev. D **86** (2012) 095031 [arXiv:1208.4018] [INSPIRE].

[48] CMS collaboration, *Measurements of properties of the Higgs boson decaying into the four-lepton final state in pp collisions at $\sqrt{s} = 13$ TeV*, JHEP **11** (2017) 047 [arXiv:1706.09936] [INSPIRE].

[49] ATLAS collaboration, *Measurement of the Higgs boson coupling properties in the $H \to ZZ^* \to 4\ell$ decay channel at $\sqrt{s} = 13$ TeV with the ATLAS detector*, JHEP **03** (2018) 095 [arXiv:1712.02304] [INSPIRE].

[50] ATLAS collaboration, *Measurement of inclusive and differential cross sections in the $H \to ZZ^* \to 4\ell$ decay channel in pp collisions at $\sqrt{s} = 13$ TeV with the ATLAS detector*, JHEP **10** (2017) 132 [arXiv:1708.02810] [INSPIRE].

[51] ATLAS collaboration, *Higgs boson production cross-section measurements and their EFT interpretation in the 4ℓ decay channel at $\sqrt{s} = 13$ TeV with the ATLAS detector*, Eur. Phys. J. C **80** (2020) 957 [*Erratum ibid.* **81** (2021) 29] [*Erratum ibid.* **81** (2021) 398] [arXiv:2004.03447] [INSPIRE].

[52] L.S. Bruni, *Polarized on Higgs? Measurement of the Higgs couplings to polarized vector bosons*, Ph.D. thesis, Twente University, Enschede (2019) DOI [INSPIRE].

[53] E. Maina, *Vector boson polarizations in the decay of the Standard Model Higgs*, Phys. Lett. B **818** (2021) 136360 [arXiv:2007.12080] [INSPIRE].

[54] E. Maina and G. Pelliccioli, *Polarized Z bosons from the decay of a Higgs boson produced in association with two jets at the LHC*, arXiv:2105.07972 [INSPIRE].

JHEP10(2021)097

[55] CMS collaboration, *Measurement of the Polarization of W Bosons with Large Transverse Momenta in W+Jets Events at the LHC*, *Phys. Rev. Lett.* **107** (2011) 021802 [arXiv:1104.3829] [INSPIRE].

[56] ATLAS collaboration, *Measurement of the polarisation of W bosons produced with large transverse momentum in pp collisions at $\sqrt{s} = 7$ TeV with the ATLAS experiment*, *Eur. Phys. J. C* **72** (2012) 2001 [arXiv:1203.2165] [INSPIRE].

[57] CMS collaboration, *Angular coefficients of Z bosons produced in pp collisions at $\sqrt{s} = 8$ TeV and decaying to $\mu^+\mu^-$ as a function of transverse momentum and rapidity*, *Phys. Lett. B* **750** (2015) 154 [arXiv:1504.03512] [INSPIRE].

[58] ATLAS collaboration, *Measurement of the angular coefficients in Z-boson events using electron and muon pairs from data taken at $\sqrt{s} = 8$ TeV with the ATLAS detector*, *JHEP* **08** (2016) 159 [arXiv:1606.00689] [INSPIRE].

[59] ATLAS collaboration, *Measurement of the W boson polarisation in $t\bar{t}$ events from pp collisions at $\sqrt{s} = 8$ TeV in the lepton + jets channel with ATLAS*, *Eur. Phys. J. C* **77** (2017) 264 [*Erratum ibid.* **79** (2019) 19] [arXiv:1612.02577] [INSPIRE].

[60] CMS collaboration, *Measurement of the W boson helicity fractions in the decays of top quark pairs to lepton + jets final states produced in pp collisions at $\sqrt{s} = 8$ TeV*, *Phys. Lett. B* **762** (2016) 512 [arXiv:1605.09047] [INSPIRE].

[61] CMS and ATLAS collaborations, *Combination of the W boson polarization measurements in top quark decays using ATLAS and CMS data at $\sqrt{s} = 8$ TeV*, *JHEP* **08** (2020) 051 [arXiv:2005.03799] [INSPIRE].

[62] ATLAS collaboration, *Measurement of $W^\pm Z$ production cross sections and gauge boson polarisation in pp collisions at $\sqrt{s} = 13$ TeV with the ATLAS detector*, *Eur. Phys. J. C* **79** (2019) 535 [arXiv:1902.05759] [INSPIRE].

[63] CMS collaboration, *Measurements of production cross sections of polarized same-sign W boson pairs in association with two jets in proton-proton collisions at $\sqrt{s} = 13$ TeV*, *Phys. Lett. B* **812** (2021) 136018 [arXiv:2009.09429] [INSPIRE].

[64] CMS collaboration, *Vector Boson Scattering prospective studies in the ZZ fully leptonic decay channel for the High-Luminosity and High-Energy LHC upgrades*, Tech. Rep. CMS-PAS-FTR-18-014, CERN, Geneva (2018).

[65] P. Azzi et al., *Report from Working Group 1*: Standard Model Physics at the HL-LHC and HE-LHC, in *Report on the Physics at the HL-LHC,and Perspectives for the HE-LHC*, A. Dainese, M. Mangano, A.B. Meyer, A. Nisati, G. Salam and M.A. Vesterinen eds., *CERN Yellow Rep. Monogr.* **7** (2019) 1 [arXiv:1902.04070] [INSPIRE].

[66] Z. Bern et al., *Left-Handed W Bosons at the LHC*, *Phys. Rev. D* **84** (2011) 034008 [arXiv:1103.5445] [INSPIRE].

[67] W.J. Stirling and E. Vryonidou, *Electroweak gauge boson polarisation at the LHC*, *JHEP* **07** (2012) 124 [arXiv:1204.6427] [INSPIRE].

[68] A. Belyaev and D. Ross, *What Does the CMS Measurement of W-polarization Tell Us about the Underlying Theory of the Coupling of W-Bosons to Matter?*, *JHEP* **08** (2013) 120 [arXiv:1303.3297] [INSPIRE].

[69] J. Baglio and N. Le Duc, *Fiducial polarization observables in hadronic WZ production: A next-to-leading order QCD+EW study*, *JHEP* **04** (2019) 065 [arXiv:1810.11034] [INSPIRE].

JHEP10(2021)097

[70] J. Baglio and L.D. Ninh, *Polarization observables in WZ production at the 13 TeV LHC: Inclusive case*, *Commun. in Phys.* **30** (2020) 35 [arXiv:1910.13746] [INSPIRE].

[71] A. Ballestrero, E. Maina and G. Pelliccioli, *W boson polarization in vector boson scattering at the LHC*, *JHEP* **03** (2018) 170 [arXiv:1710.09339] [INSPIRE].

[72] A. Ballestrero, E. Maina and G. Pelliccioli, *Polarized vector boson scattering in the fully leptonic WZ and ZZ channels at the LHC*, *JHEP* **09** (2019) 087 [arXiv:1907.04722] [INSPIRE].

[73] A. Ballestrero, E. Maina and G. Pelliccioli, *Different polarization definitions in same-sign WW scattering at the LHC*, *Phys. Lett. B* **811** (2020) 135856 [arXiv:2007.07133] [INSPIRE].

[74] A. Ballestrero, A. Belhouari, G. Bevilacqua, V. Kashkan and E. Maina, *PHANTOM: A Monte Carlo event generator for six parton final states at high energy colliders*, *Comput. Phys. Commun.* **180** (2009) 401 [arXiv:0801.3359] [INSPIRE].

[75] J. Alwall et al., *The automated computation of tree-level and next-to-leading order differential cross sections, and their matching to parton shower simulations*, *JHEP* **07** (2014) 079 [arXiv:1405.0301] [INSPIRE].

[76] C.F. Uhlemann and N. Kauer, *Narrow-width approximation accuracy*, *Nucl. Phys. B* **814** (2009) 195 [arXiv:0807.4112] [INSPIRE].

[77] P. Artoisenet, R. Frederix, O. Mattelaer and R. Rietkerk, *Automatic spin-entangled decays of heavy resonances in Monte Carlo simulations*, *JHEP* **03** (2013) 015 [arXiv:1212.3460] [INSPIRE].

[78] D. Buarque Franzosi, O. Mattelaer, R. Ruiz and S. Shil, *Automated predictions from polarized matrix elements*, *JHEP* **04** (2020) 082 [arXiv:1912.01725] [INSPIRE].

[79] A. Denner and G. Pelliccioli, *Polarized electroweak bosons in W^+W^- production at the LHC including NLO QCD effects*, *JHEP* **09** (2020) 164 [arXiv:2006.14867] [INSPIRE].

[80] A. Denner and G. Pelliccioli, *NLO QCD predictions for doubly-polarized WZ production at the LHC*, *Phys. Lett. B* **814** (2021) 136107 [arXiv:2010.07149] [INSPIRE].

[81] R. Poncelet and A. Popescu, *NNLO QCD study of polarised W^+W^- production at the LHC*, *JHEP* **07** (2021) 023 [arXiv:2102.13583] [INSPIRE].

[82] D.Y. Bardin, A. Leike, T. Riemann and M. Sachwitz, *Energy Dependent Width Effects in e^+e^- Annihilation Near the Z Boson Pole*, *Phys. Lett. B* **206** (1988) 539 [INSPIRE].

[83] R.G. Stuart, *General renormalization of the gauge invariant perturbation expansion near the Z^0 resonance*, *Phys. Lett. B* **272** (1991) 353 [INSPIRE].

[84] R.G. Stuart, *Gauge invariance, analyticity and physical observables at the Z^0 resonance*, *Phys. Lett. B* **262** (1991) 113 [INSPIRE].

[85] A. Denner, S. Dittmaier, M. Roth and L.H. Wieders, *Electroweak corrections to charged-current $e^+e^- \to 4$ fermion processes: Technical details and further results*, *Nucl. Phys. B* **724** (2005) 247 [*Erratum ibid.* **854** (2012) 504] [hep-ph/0505042] [INSPIRE].

[86] A. Denner, S. Dittmaier, M. Roth and D. Wackeroth, *Electroweak radiative corrections to $e^+e^- \to WW \to 4$ fermions in double-pole approximation: The RACOONWW approach*, *Nucl. Phys. B* **587** (2000) 67 [hep-ph/0006307] [INSPIRE].

JHEP10(2021)097

[87] A. Denner and S. Dittmaier, *Electroweak Radiative Corrections for Collider Physics*, *Phys. Rept.* **864** (2020) 1 [arXiv:1912.06823] [INSPIRE].

[88] A. Denner, S. Dittmaier and M. Roth, *Non-factorizable photonic corrections to $e^+e^- \to WW \to$ four fermions*, *Nucl. Phys. B* **519** (1998) 39 [hep-ph/9710521] [INSPIRE].

[89] W. Beenakker, A.P. Chapovsky and F.A. Berends, *Nonfactorizable corrections to W pair production: Methods and analytic results*, *Nucl. Phys. B* **508** (1997) 17 [hep-ph/9707326] [INSPIRE].

[90] S. Dittmaier and C. Schwan, *Non-factorizable photonic corrections to resonant production and decay of many unstable particles*, *Eur. Phys. J. C* **76** (2016) 144 [arXiv:1511.01698] [INSPIRE].

[91] S. Catani and M.H. Seymour, *A general algorithm for calculating jet cross-sections in NLO QCD*, *Nucl. Phys. B* **485** (1997) 291 [*Erratum ibid.* **510** (1998) 503] [hep-ph/9605323] [INSPIRE].

[92] S. Dittmaier, *A general approach to photon radiation off fermions*, *Nucl. Phys. B* **565** (2000) 69 [hep-ph/9904440] [INSPIRE].

[93] S. Catani, S. Dittmaier, M.H. Seymour and Z. Trócsányi, *The dipole formalism for next-to-leading order QCD calculations with massive partons*, *Nucl. Phys. B* **627** (2002) 189 [hep-ph/0201036] [INSPIRE].

[94] A. Denner, J.-N. Lang and M. Pellen, *Full NLO QCD corrections to off-shell $t\bar{t}b\bar{b}$ production*, *Phys. Rev. D* **104** (2021) 056018 [arXiv:2008.00918] [INSPIRE].

[95] J.M. Cornwall, D.N. Levin and G. Tiktopoulos, *Derivation of Gauge Invariance from High-Energy Unitarity Bounds on the S Matrix*, *Phys. Rev. D* **10** (1974) 1145 [*Erratum ibid.* **11** (1975) 972] [INSPIRE].

[96] C.E. Vayonakis, *Born Helicity Amplitudes and Cross-Sections in Nonabelian Gauge Theories*, *Lett. Nuovo Cim.* **17** (1976) 383 [INSPIRE].

[97] M.S. Chanowitz and M.K. Gaillard, *The TeV Physics of Strongly Interacting W's and Z's*, *Nucl. Phys. B* **261** (1985) 379 [INSPIRE].

[98] G.J. Gounaris, R. Kögerler and H. Neufeld, *Relationship Between Longitudinally Polarized Vector Bosons and their Unphysical Scalar Partners*, *Phys. Rev. D* **34** (1986) 3257 [INSPIRE].

[99] M.J. Duncan, *Higgs detection via Z^0 polarization*, *Phys. Lett. B* **179** (1986) 393 [INSPIRE].

[100] S.S.D. Willenbrock, *Pair Production of W and Z Bosons and the Goldstone Boson Equivalence Theorem*, *Annals Phys.* **186** (1988) 15 [INSPIRE].

[101] S. Actis, A. Denner, L. Hofer, A. Scharf and S. Uccirati, *Recursive generation of one-loop amplitudes in the Standard Model*, *JHEP* **04** (2013) 037 [arXiv:1211.6316] [INSPIRE].

[102] S. Actis, A. Denner, L. Hofer, J.-N. Lang, A. Scharf and S. Uccirati, *RECOLA: REcursive Computation of One-Loop Amplitudes*, *Comput. Phys. Commun.* **214** (2017) 140 [arXiv:1605.01090] [INSPIRE].

[103] A. Denner, S. Dittmaier and L. Hofer, *Collier: a fortran-based Complex One-Loop LIbrary in Extended Regularizations*, *Comput. Phys. Commun.* **212** (2017) 220 [arXiv:1604.06792] [INSPIRE].

JHEP10(2021)097

[104] Particle Data Group collaboration, *Review of Particle Physics*, *Phys. Rev. D* **98** (2018) 030001 [INSPIRE].

[105] A. Denner and S. Dittmaier, *The complex-mass scheme for perturbative calculations with unstable particles*, *Nucl. Phys. B Proc. Suppl.* **160** (2006) 22 [hep-ph/0605312] [INSPIRE].

[106] A. Buckley et al., *LHAPDF6: parton density access in the LHC precision era*, *Eur. Phys. J. C* **75** (2015) 132 [arXiv:1412.7420] [INSPIRE].

[107] NNPDF collaboration, *Parton distributions from high-precision collider data*, *Eur. Phys. J. C* **77** (2017) 663 [arXiv:1706.00428] [INSPIRE].

[108] NNPDF collaboration, *Illuminating the photon content of the proton within a global PDF analysis*, *SciPost Phys.* **5** (2018) 008 [arXiv:1712.07053] [INSPIRE].

[109] M. Cacciari, G.P. Salam and G. Soyez, *The anti-k_t jet clustering algorithm*, *JHEP* **04** (2008) 063 [arXiv:0802.1189] [INSPIRE].

[110] Z. Nagy and Z. Trócsányi, *Next-to-leading order calculation of four jet observables in electron positron annihilation*, *Phys. Rev. D* **59** (1999) 014020 [*Erratum ibid.* **62** (2000) 099902] [hep-ph/9806317] [INSPIRE].

JHEP10(2021)097